From Graphene Oxide to Graphene: Changes in Interfacial Water Structure and Reactivity Using Deep Neural Network Force Fields

Golam Azom,[a] Anne Milet,[b] Rolf David,[a,c*] and Revati Kumar[a*]

[a]Department of Chemistry, Louisiana State University, Baton Rouge, Louisiana 70803-1804, United States.

[b]Department of Chemistry, University of Grenoble Alpes, 38400 Saint-Martin-d'Hères, France

[c]Current affiliation: PASTEUR, Department of Chemistry, École Normale Supérieure, PSL University, Sorbonne Université, CNRS, 75005 Paris, France

*E-mail: revatik@lsu.edu, rolf.david@ens.psl.eu

Abstract

Graphene oxides (GO) are thin graphene sheets containing oxygen-bearing defects. These sheets have a complex structure with sp^3 carbons interspersed among sp^2 carbons, which results in competition between aromatic and hydrophilic domains at the GO-water interface. The GO-water as well as neat graphene-water interfacial regions play a crucial role in various applications. While *ab-initio* molecular dynamics simulations provide high accuracy in studying this complex region, they require significant computational resources, which limits the investigation of the interface at both time and length scales. To tackle this issue, a deep neural network forcefield (DNNF), trained and validated on AIMD data, was developed. It achieves DFT-level accuracy using only a fraction of the computational cost. This DNNF has been successfully used for simulating graphene oxide to reduced graphene oxide right up to fully reduced graphene-water interfaces. The ordering of water near the interface was studied as a function of oxidation level from fully oxidized graphene oxide to graphene. The vibrational sum frequency generation spectrum of the graphene-water interface was determined and compared to experimental data as well as spectra from graphene oxide-water sheets at different oxidation levels. Connections between different spectral signatures and the orientation of different waters were determined. The reactivity and buckling of the different sheets were examined. The analyses of the trajectories revealed the formation of multiple hydronium formation events with sustained proton hopping over more than a 100 ps in the fully oxidized GO-water systems.

I. Introduction

Graphene and its derivative, graphene oxide (GO), stand out as highly promising nanomaterials because of their scope in numerous applications. The field of graphene oxide (GO) has garnered much attention in recent years due to its potential in a variety of applications including catalysis,[1-4] gas[5] and water purification,[6-15] separations[16-18], and energy storage devices[19-25] among others. Especially in the realm of adsorbent applications, GO is experiencing a surge in popularity because of its high efficiency and low risk.[26] GO is widely used in rare earth separations,[9, 16, 26] radionuclide decontaminations (Lu(III), Eu(III), Th(IV), Np(V), U(VI), etc.),[26-29] and desalination.[30] While graphene is made of sp^2 hybridized carbons, GO is composed of graphene sheets that have been modified with oxygenated functional groups like hydroxyls, epoxides,[20] carboxylic acids,[31] or sulfonate groups.[3, 32] These oxygenated functional groups are believed to play a crucial role in efficiently adsorbing radionuclides.[33] In a study, Tan *et al.* reported that the adsorption of Cs(I) on GO was an exothermal and spontaneous process.[34] In aqueous environments, the GO-liquid interface displays unique phenomena due to differences in structure and dynamics compared to the bulk condensed phase. This asymmetry affects the material's reactivity, transport, conductivity, and adsorption properties, making it essential to have a molecular-level understanding of water at the GO interfaces to design GO materials for specific applications. The orientation of water and ions near interfaces can often be significantly different than the bulk.[35, 36] Understanding water and ion organization near interfaces is crucial for pioneering advancements in adsorbent technology.[37] Although there are numerous experimental studies regarding GO as an adsorbent, most of them use bulk experimental techniques[9, 26, 28] while a few of them probed the interface directly.[18, 38] Probing interfaces experimentally is challenging

as the interfacial region is significantly smaller and hence requires surface-specific experiments.[37] Molecular dynamics simulations act as direct probes of these complex interfacial regions.

Vibrational Sum-Frequency Generation (vSFG) is a powerful tool for probing interfaces,[39-43] and when used in conjunction with complementary molecular simulations, it can provide a molecular-level picture of interfacial solvation environments.[44-49] Molecular dynamics simulations can be used to obtain both vSFG spectra and other structural properties in situ. Reactive events occurring at the interfaces of air-water[50-52] and GO-water[53] have been reported in the literature. Using conventional molecular dynamics (MD) force fields to generate vSFG spectra and capture reactive events is not ideal, because it assumes a constant bonding topology throughout the simulation. In contrast, *ab-initio* molecular dynamics (AIMD)[54] simulation calculates the forces on the nuclei without assuming a bond topology, explicitly treating electronic degrees of freedom. This makes AIMD well-suited for capturing reactive events and obtaining surface-specific vSFG spectra. However, AIMD is computationally expensive, limiting its applicability to GO-liquid interfaces containing only a few hundred atoms and timescales of around a hundred picoseconds. While a 100 ps simulation can provide vSFG spectra using velocity-velocity autocorrelation based methods, a longer simulation is required to observe reactive events at the GO-water interface.[53] David *et al.* observed the formation of a proton at GO-water interfaces, which subsequently travels to the bulk water region.[53] One key interest lies in understanding how the proton transports over time - whether it migrates to air-water interfaces or returns to the GO-water interface, and the effect of these interfaces on dynamical properties such as the proton hopping rate.

The pursuit of bridging the gap between the accuracy of *ab-initio* molecular dynamics (AIMD) and the computational efficiency of empirical force fields has led to the widespread use of machine learning-based techniques. These techniques aim to replicate the potential energy

surface (PES) of a system of interest by utilizing data generated from highly accurate first principle (*e.g.* DFT) calculations. This approach has proven to be effective in achieving a balance between computational efficiency and accuracy in modeling molecular systems.[55-57] Over the years, various models have been developed to construct machine learning (ML) potentials, falling into two main categories: the kernel-based methods, such as Gradient Domain Machine Learning (GDML) model[58] or Gaussian Approximation Potentials (GAPs)[57], and the Neural Networks Potentials methods. The Neural Networks Potentials encompasses the Behler-Parinello High Dimensional Neural Network Potentials (HDNNPs),[59, 60] Deep Potential Molecular Dynamics (DeePMD),[61-63] and E(3)-Equivariant Graph Neural Network[64] among others. Among these models, DeePMD, which utilizes an end-to-end neural network architecture to predict potential energies and forces, has gained significant attention due to its high accuracy in reproducing the reference *ab-initio* data used for training while being several orders of magnitude faster.[65]

In recent years, DeePMD has become a very powerful tool for studying interfaces, such as the rutile TiO_2-water interface,[66, 67] Li-Cu interface,[68] water in graphene nanocapillaries,[69] the air-water interface,[70-72] and many more. Additionally, this method has proven useful in capturing reactive events.[73-75]

In this work, a Deep Neural Network Forcefield (DNNF) was developed for aqueous graphene oxide interface using data from *ab-initio* molecular dynamics of the GO-water interface at two different oxidation levels (fully oxidized and partially reduced) as initial training dataset which was then enriched within an active learning scheme. This force field was then used to simulate the GO water interface at different oxidation levels, at increased time and length scales. To validate the force field, the accuracy of force prediction on the test dataset was determined along with different structural properties (density profile, radial distribution function, orientation

of interfacial water molecules, fluctuation of GO sheet, hydrogen bonding environments), and vSFG spectra were calculated and compared with *ab-initio* simulations. The force field was also used to simulate three different GO-water interfaces and graphene-water interfaces, and force prediction for all these systems was evaluated. The vSFG spectra obtained for the graphene-water interface were compared with experimental results. Reactive events at different GO interfaces were investigated, focusing on the proton transport events at longer timescales than timescales available by AIMD simulation while preserving its accuracy.

The paper is divided into four sections. After this introduction, the methods are outlined in section II. The validation of the DNNF is presented in Section III A. The results on the extension of the DNNF simulations to other GO and graphene-water systems, from interfacial water orientation to reactive events to spectroscopic investigations, are presented and discussed in Section III B. Finally, the conclusions are summarized in section IV.

II. Methods

As mentioned in the introduction, DeePMD was used to develop DNNF for the graphene oxide systems. The parameterization data was taken from AIMD simulations of graphene oxide-water systems for two different GO sheets (see Figure 1 for the two sheets under study and the simulation setup and Supporting Information for the details of the simulations) one that is fully oxidized, $GO_{2/1}$ (with a carbon to oxygen ratio of 2:1), and a partially oxidized sheet, $GO_{4/1}$ (with a carbon to oxygen ration of 4:1).

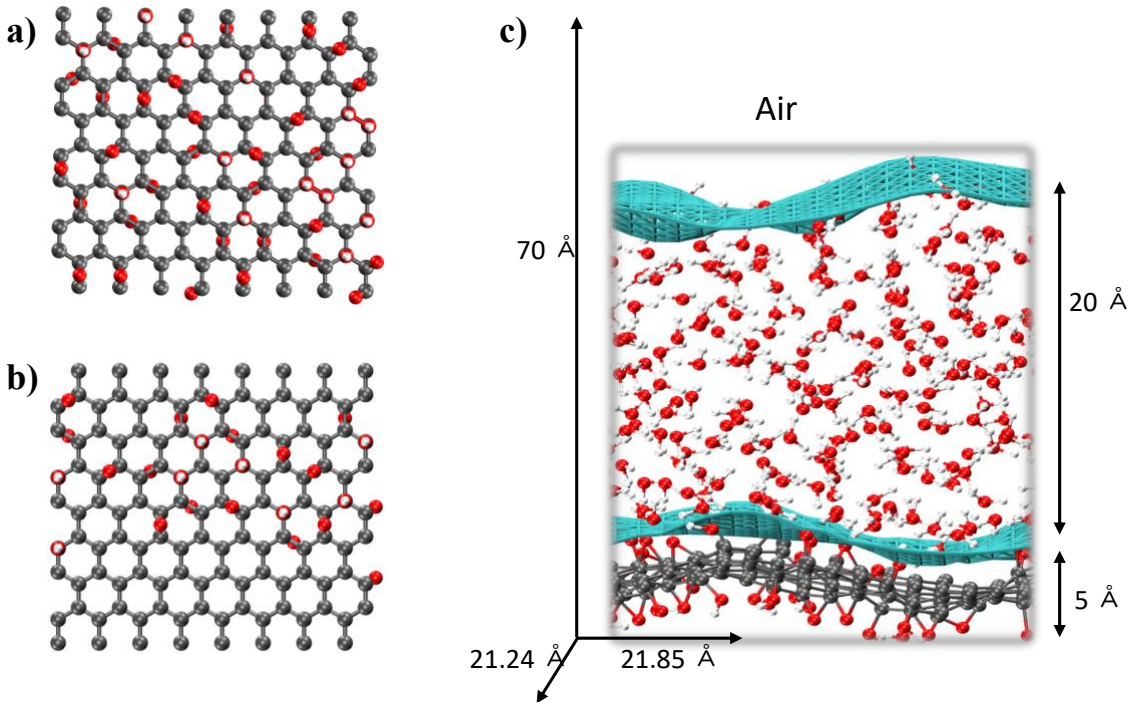

Figure 1. Schematic representation of a) $GO_{2/1}$ sheet, b) $GO_{4/1}$ sheet, c) $GO_{4/1}$-water system. Carbons, oxygens, and hydrogens are represented in grey, red, and white colors. Both GO-water interface (bottom) and air-water instantaneous water interface (top) are shown in cyan color.

Details of the reference data used in the construction of the initial training dataset, followed by a concise overview of the iterative training process of the DNNF (see Figure S1 for a flowchart for

the training procedure) and detailed information on the various graphene oxide/graphene sheets are provided in the Supporting Information (S1). Finally, new simulation boxes were set up for each GO system under study with a larger number of water molecules (see Figure S2). The trajectories from these larger simulations were analyzed and the details of the analyses conducted on the simulated trajectories are provided below.

i. *Average Water Density from the Instantaneous Interface*

The dynamical interface between GO and water was characterized by calculating the Willard-Chandler instantaneous water interface[76]. The average water density, divided by the bulk value, was calculated as a function of distance from the instantaneous water interface, (ρ/ρ_{bulk}), to gain insight into the structure of the different interfacial water layers. In previous work, David *et al.* have shown distinct interfacial regimes for GO-water systems and this method has also been used by Gaigeot *et al.*[77] to study various solid-liquid interfaces.

ii. *Orientation of Water Molecules*

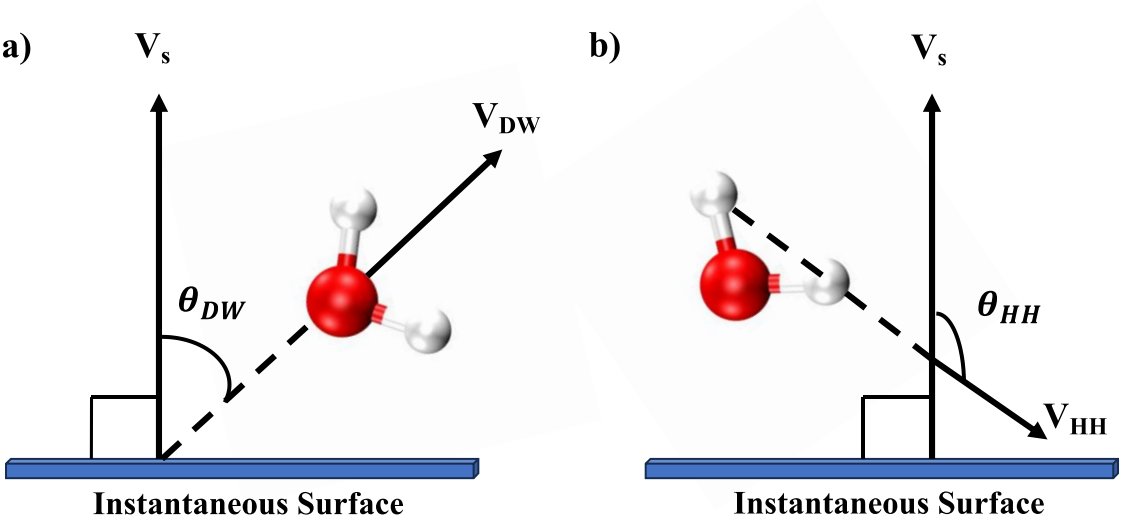

Figure 2. Schematic of water orientational angle a) θ_{DW}, b) θ_{HH}. Note that the schematic instantaneous surface shown here is constructed using the three closest points from the water molecule on the instantaneous surface.

The orientation of a water molecule with respect to the instantaneous surface was investigated by calculating the joint distribution of two angles: θ_{DW} and θ_{HH}.[47] θ_{DW} was defined as the angle between the water bisector V_{DW} and the normal vector to the instantaneous water surface V_s (always pointing in the direction of the water molecule) while θ_{HH} was defined as the angle between the vector connecting two H atoms of a water molecule V_{HH} and the normal vector to the instantaneous water surface V_s, always pointing in the direction of the water (see Figure 2). To compute the surface normal vector, the closest three points on the instantaneous surface from the water oxygen were selected and the normal vector was defined as the vector perpendicular to the plane formed by these three points.

iii. Hydrogen Bond Analysis

The hydrogen bonding environment of the interfacial water molecules was examined. A hydrogen bond is defined when the distance (r) between the hydrogen of donor species and the oxygen of acceptor species is less than 2.5 Å.[78-80] To classify the hydrogen bond classes, a naming scheme developed from the work of Kumar *et al.*[78] and used by David *et al.*[47] was employed. In this study, water molecules were classified as a part of class **Nx**, where **N** is the total number of hydrogen bonds for a particular water molecule, and **X** is the number of hydrogen bonds associated with the H atoms (donor) of the water molecule under consideration. Specifically, **X** was denoted as S for single donor, D for double donor, and T for triple donor water. Both water-water and water-functional group hydrogen bonds were considered.

iv. vibrational Sum-Frequency Generation Spectra

The computation of the vibrational Sum-Frequency Generation (vSFG) spectra of O-H stretch mode in water from simulations was performed using the surface-specific velocity-velocity autocorrelation function (ssVVCF) formalism proposed by Ohto *et al.*[81] The benefit of using this formalism is that it does not require long trajectories to converge. In the ssVVCF algorithm, the resonant part of the SFG response function, $\chi_{xxz}^{(2),R}(\omega)$ can be written as

$$\chi_{xxz}^{(2),R}(\omega) = \frac{Q(\omega)\mu(\omega)\alpha(\omega)}{i\omega^2}\int_0^\infty dt e^{-i\omega t} \times \langle \sum_{i,j} g\left(r_{ij}(0)\right)\dot{r}_{z,i}^{OH}(0)\frac{\dot{\vec{r}}_j^{OH}(t)\,.\,\vec{r}_j^{OH}(t)}{|\vec{r}_j^{OH}(t)|}\rangle \qquad (1)$$

Here $\dot{r}_{z,i}^{OH}$ is the z component of the velocity of the i^{th} water OH vector, $\dot{\vec{r}}_j^{OH}$ and $\vec{r}_j^{OH}$ is the velocity vector and displacement vector of the j^{th} water OH respectively. $Q(\omega)$ is the quantum correction factor expressed by[82]

$$Q(\omega) = \frac{\beta\hbar\omega}{1 - e^{-\beta\hbar\omega}} \qquad (2)$$

where $\beta = \frac{1}{kT}$ and $\hbar$ is the reduced Planck constant. The function $g(r_{ij})$ in equation 1 was used as a switching function to control the cross-correlation terms between the O-H stretch chromophores (*i* and *j*) where r_{ij} is the distance between the center of mass of the chromophores *i* and *j*

$$g(r_{ij}) = \begin{cases} 1, & r_{ij} \leq 2\ \text{Å} \\ 0, & r_{ij} > 2\ \text{Å} \end{cases} \qquad (3)$$

To ensure that only intramolecular coupling terms were considered, a cutoff of 2 Å was used (intermolecular coupling was neglected due to convergence issues in relatively short AIMD trajectories that are the reference data for this work). The non-Condon effects were accounted for through the inclusion of frequency-dependent transition dipole moment $\mu(\omega)$ and polarizability $\alpha(\omega)$, both of which are parameterized by Corcelli and Skinner[83, 84] given by

$$\mu(\omega) = \left(1.377 + \frac{53.03(3737.0 - \omega)}{6932.2}\right)\mu^0 \qquad (4)$$

$$\alpha(\omega) = \left(1.271 + \frac{6.287(3737.0 - \omega)}{6932.2}\right)\alpha^0 \qquad (5)$$

A smoothing Hann window function was applied to the Fourier transform of the time correlation function with a time cutoff of 0.50 ps

$$f(t) = \begin{cases} cos^2\left(\frac{\pi}{2\tau}\right), & 0 < t < \tau \\ 0, & t > \tau \end{cases} \qquad (6)$$

v. Proton hopping function H(t)

In the cases wherein a hydronium ion was formed from a proton transfer event from the sheet to an interfacial water, the Grotthuss shuttling of the proton over different water molecules as a function of time was studied and quantified using the proton hopping function, H(t). The definition of H(t) is derived from the work of Voth *et al*.[50, 85] and used by David and Kumar[53] for the GO-water system. Each hydrogen is bonded to its nearest heavy atom. A hydronium ion is defined as an O atom with 3 H atoms bonded to it. The time origin is set to 0 at the time step when the hydronium is formed. In the subsequent time step, if the identity of the O atom of the hydronium remains the same, then the function H(Δt) remains the same. Hence at any time t+Δt, if the identity of the hydronium O atom is the same then H(t+Δt) = H(t). If, however, the O atom of the hydronium at time t +Δt is not the same as at time t, then there are two cases.

i) The O atom of the new hydronium is different from the five previous hydroniums with distinctly different O atoms, then H(t) is increased by 1.

ii) If the new hydronium has the same O atom as one of the previous five hydroniums, then H(t) is decreased by m, where m is 1 if it is the previous O atom, 2 if it is the O atom before that, and so on until m=5.

III. Results and Discussions

A. Validation of the DNNF

In order to test the robustness of the developed DNNF, it was validated on different sets of data. The ability of the DNNF to reproduce the *ab initio* forces on not just test data sets for the systems that were used for development but also for the systems at different temperatures as well as sheets with different oxidation levels was first evaluated. The results of the ability of the DNNF in force prediction can be found in the Supporting Information (Figures S3-S6). Next, the trajectories from DNNF simulations were analyzed to check the accuracy of the force-field to reproduce the AIMD GO-water interfacial structure. Specifically, in the following section the interfacial water orientation, structure, reactivity, and spectra from DNNF simulations are compared to results from AIMD.

i. Average water density profile and pair correlation function

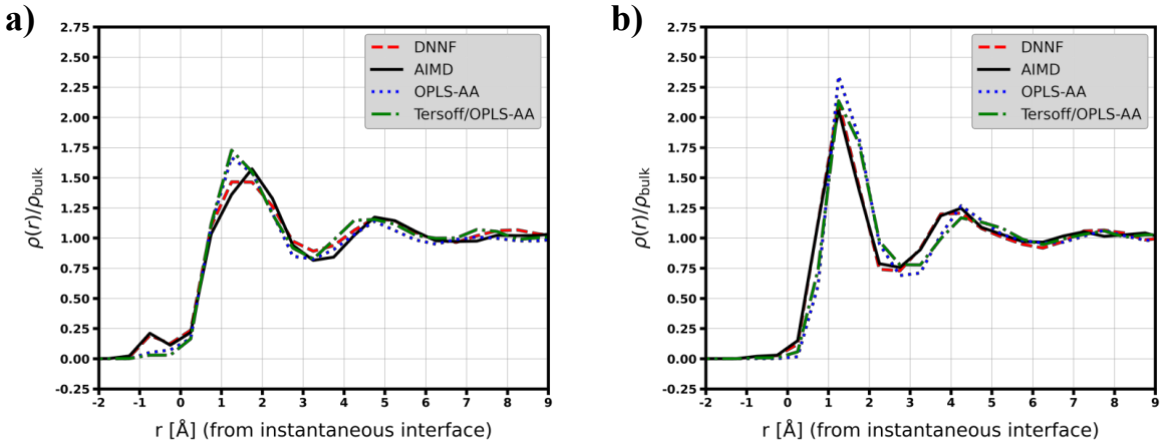

Figure 3. Average water density as a function of distance from the instantaneous interface using AIMD, DNNF, OPLS-AA, and Tersoff/OPLS-AA for a) $GO_{2/1}$-water, b) $GO_{4/1}$-water.

The density profile in Figure 3 provides valuable information about the interfacial water structure. The ratio of water density to bulk water density is reported as a function of distance from the instantaneous water surface using four different force-fields. A hybrid OPLS-AA/Tersoff was used to model GO and the SPC/E force-field for water and the results were compared to the DNNF result. This hybrid force-field chosen as it gave reasonable agreement with the interfacial water orientations at the interface compared to AIMD data, as shown by Don et al.[15] The simulation details using the Tersoff and OPLS-AA forcefield can be found in the SI (S2). Based on the location of the minima, water layers are classified into three categories: L1, L2, and L3 layers, which correspond to the first, second, and third minima, respectively. Notably, for $GO_{2/1}$-water, a small shoulder is observed at the negative region of the instantaneous water interface (L0 layer) from both AIMD and DNNF, but it is absent in OPLS-AA and Tersoff/OPLS-AA. In the case of $GO_{2/1}$, the L1 layer is located at 3.25 Å for AIMD, DNNF, OPLS-AA, and Tersoff/OPLS-AA. The first peak position varies depending on the force-field. AIMD gives a first peak at 1.75 Å, while DNNF gives a wide first peak centered at 1.5 Å. OPLS-AA and Tersoff/OPLS-AA have sharper peaks at 1.25 Å. The L2 layer is located at 6.75 Å for both AIMD and DNNF, whereas in OPLS-AA and Tersoff/OPLS-AA this layer is positioned at 6.25 Å. For $GO_{4/1}$, the L1 layer is located at 2.75 Å for AIMD, DNNF, and OPLS-AA while Tersoff/OPLS-AA gives the minima at 3.25 Å. The first peak is at 1.25 Å with the same intensity for AIMD, DNNF, and Tersoff/OPLS-AA while OPLS-AA gives the first peak at 1.25 Å with higher intensity. Overall, the DNNF closely resembles the layering and water structure of AIMD, compared to OPLS-AA and Tersoff/OPLS-AA.

Further validation can be seen in Figure S7, which presents the radial distribution function (g(r)) for elemental pairs (C-C, C-O, C-H, O-O, O-H, H-H) in both $GO_{2/1}$-water and $GO_{4/1}$-water.

DNNF reproduces the radial distribution functions of AIMD with high accuracy, while OPLS-AA and Tersoff/OPLS-AA do not.

ii. Orientation of interfacial water molecules

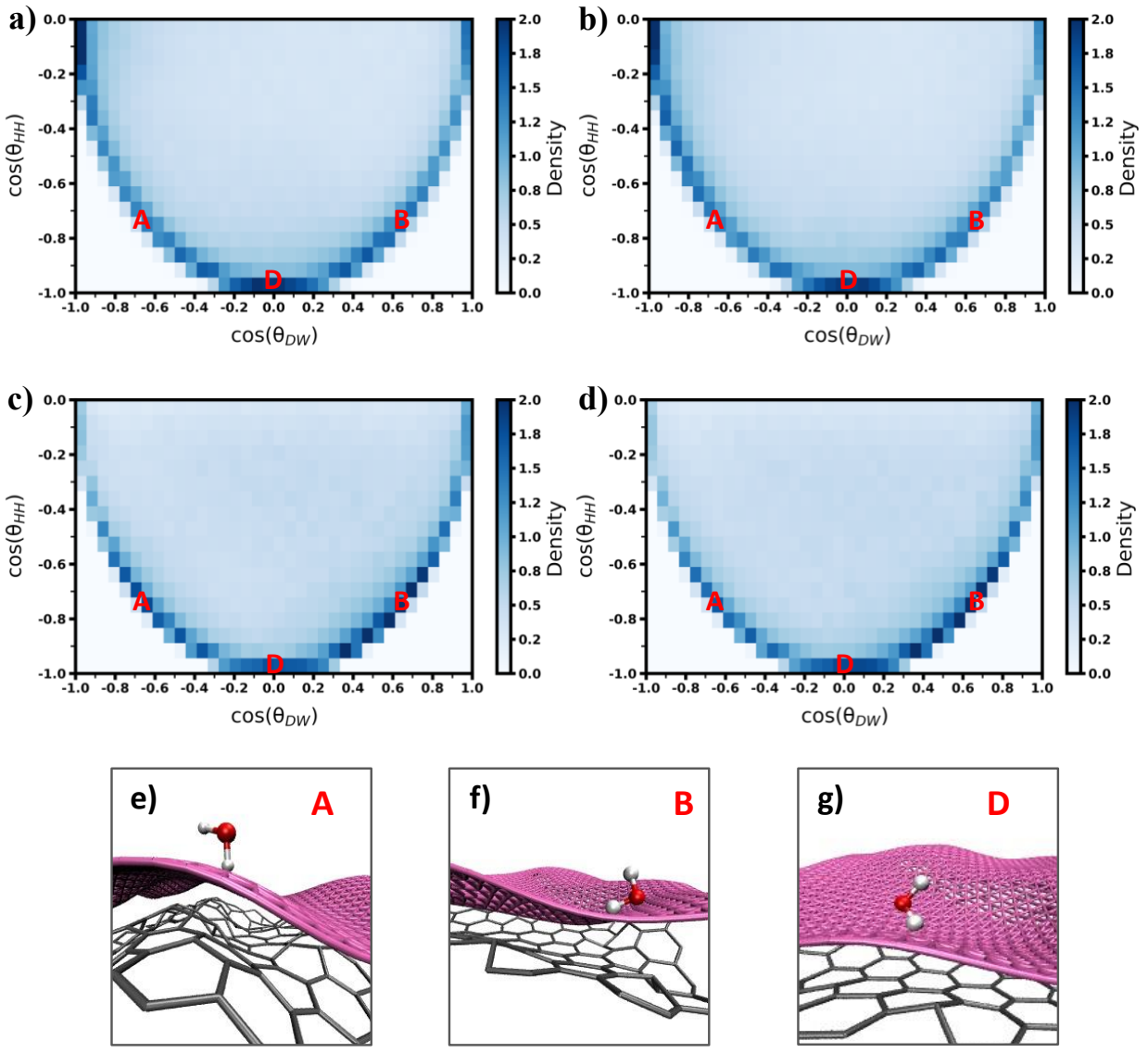

Figure 4. Two-dimensional joint probability density distribution of $\cos(\theta_{DW})$ and $\cos(\theta_{HH})$ for $GO_{2/1}$-water L1 layer using a) AIMD, b) DNNF, c) OPLS-AA, d) Tersoff/OPLS-AA. Representative orientations of water molecules e) $\cos(\theta_{DW})$/$\cos(\theta_{HH})$ pair values equal to -0.71/-

0.69 (**A**), f) $\cos(\theta_{DW})/\cos(\theta_{HH})$ pair values equal to 0.64/-0.71 (**B**), g) $\cos(\theta_{DW})/\cos(\theta_{HH})$ pair values equal to 0.03/-0.99 (**D**).

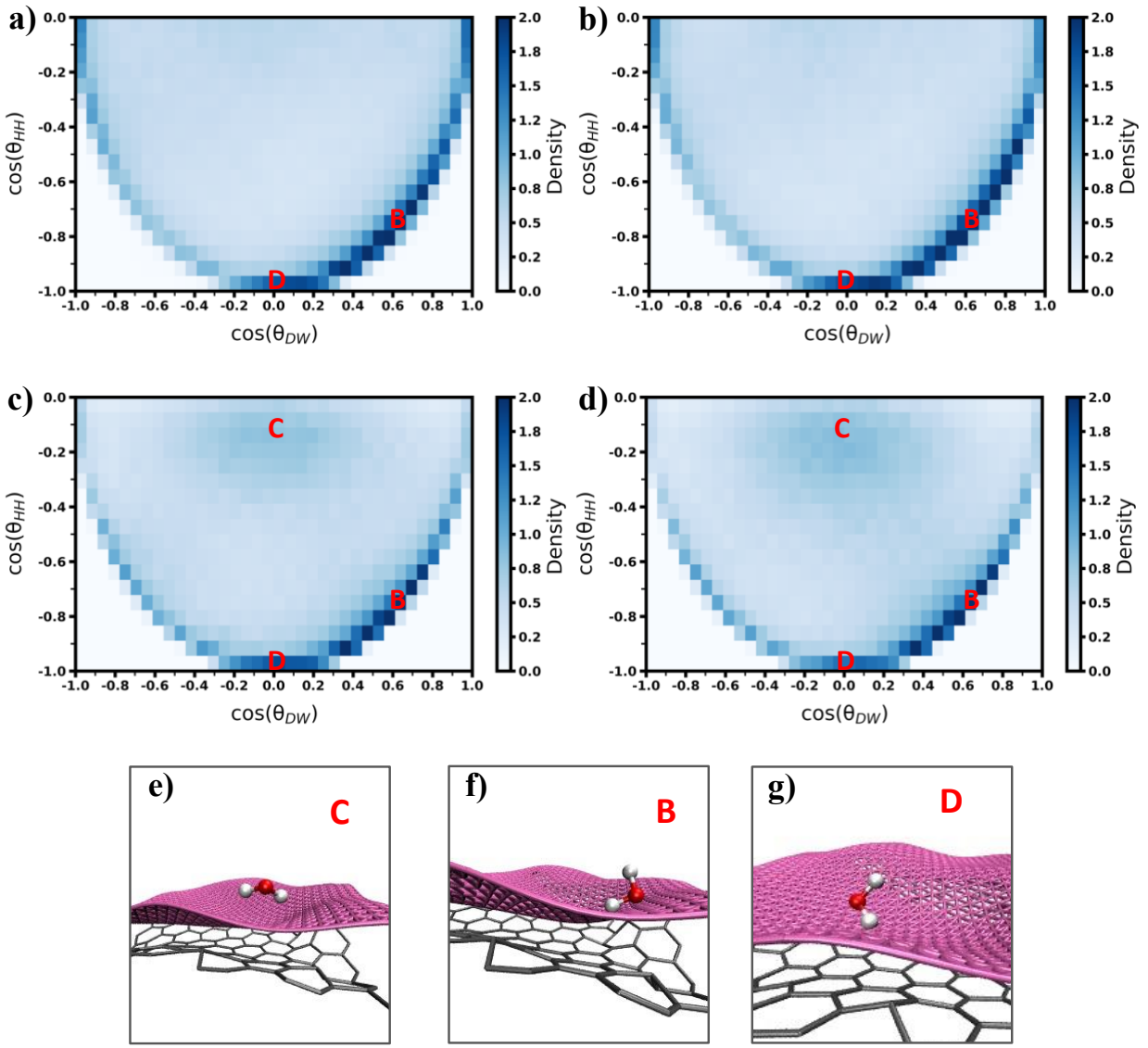

Figure 5. Joint probability density distribution of $\cos(\theta_{DW})$ and $\cos(\theta_{HH})$ for $GO_{4/1}$-water L1 layer using a) AIMD, b) DNNF, c) OPLS-AA, d) Tersoff/OPLS-AA. Representative orientations of water molecules e) $\cos(\theta_{DW})/\cos(\theta_{HH})$ pair values equal to -0.09/-0.09 (**C**), f) $\cos(\theta_{DW})/\cos(\theta_{HH})$ pair values equal to 0.64/-0.71 (**B**), g) $\cos(\theta_{DW})/\cos(\theta_{HH})$ pair values equal to 0.03/-0.99 (**D**).

In order to form a better understanding of the orientation of water molecules at the interface between graphene oxide and water, the orientation of L1 water was analyzed. Figures 4 and 5 show the joint distribution of $\cos(\theta_{DW})$/$\cos(\theta_{HH})$ angles for $GO_{2/1}$ and $GO_{4/1}$ in the L1 layer evaluated using AIMD, DNNF, OPLS-AA, and Tersoff/OPLS-AA. For $GO_{2/1}$, there are three significant orientation peaks for AIMD; one ranging from 0.57 to 0.64 and from -0.71 to -0.77 for $\cos(\theta_{DW})$ and $\cos(\theta_{HH})$, respectively and represents region **B** (one water OH pointing away from the interface). The second peak ranges from -0.71 to -0.77 and from -0.64 to -0.71 for $\cos(\theta_{DW})$ and $\cos(\theta_{HH})$, respectively and represent region **A** (one water OH pointing towards the interface). The third peak is centered at 0 and -0.98 for $\cos(\theta_{DW})$ and $\cos(\theta_{HH})$, respectively, and represents region **D** (one water OH pointing away and another OH pointing toward the interface). The DNNF method successfully reproduces three major peaks from AIMD with the same intensity, as shown in Figure 4.a and 4.b. However, OPLS-AA and Tersoff/OPLS-AA exhibit slightly higher intensity for two major peaks (regions **A** and **B**) as shown in Figures 4.c and 4.d. In addition, there is an intense distribution centered at -0.97 and -0.1(both water OH pointing towards the interface) for $\cos(\theta_{DW})$ and $\cos(\theta_{HH})$, respectively in both AIMD and DNNF which is absent in OPLS-AA and Tersoff/OPLS-AA. For $GO_{4/1}$, there are two major peaks in regions **B** and **D** (Figure 5.a and 5.b) for both AIMD and DNNF. However, for OPLS-AA and Tersoff/OPLS-AA, the major peak in region **B** is not as widely distributed as it is in AIMD (Figure 5.c and 5.d). Additionally, they have two minor peaks, one in region **A** and another in region **C** (both water OH parallel to the interface) which range from -0.08 to -0.17 and from -0.08 to -0.17 for $\cos(\theta_{DW})$ and $\cos(\theta_{HH})$, respectively. These minor peaks are not observed in AIMD. To provide clarity and compare the distributions of each force field with AIMD, a difference plot is included in the supporting information (Figure S8). In both $GO_{2/1}$ and $GO_{4/1}$, the distribution difference is noteworthy for both OPLS-AA and

Tersoff/OPLS-AA, while the variance is minimal in the case of DNNF. This observation highlights that DNNF accurately reproduces the water orientation at the interfacial layer as seen in AIMD simulations for both $GO_{2/1}$ and $GO_{4/1}$.

iii. vibrational Sum-frequency generation spectra

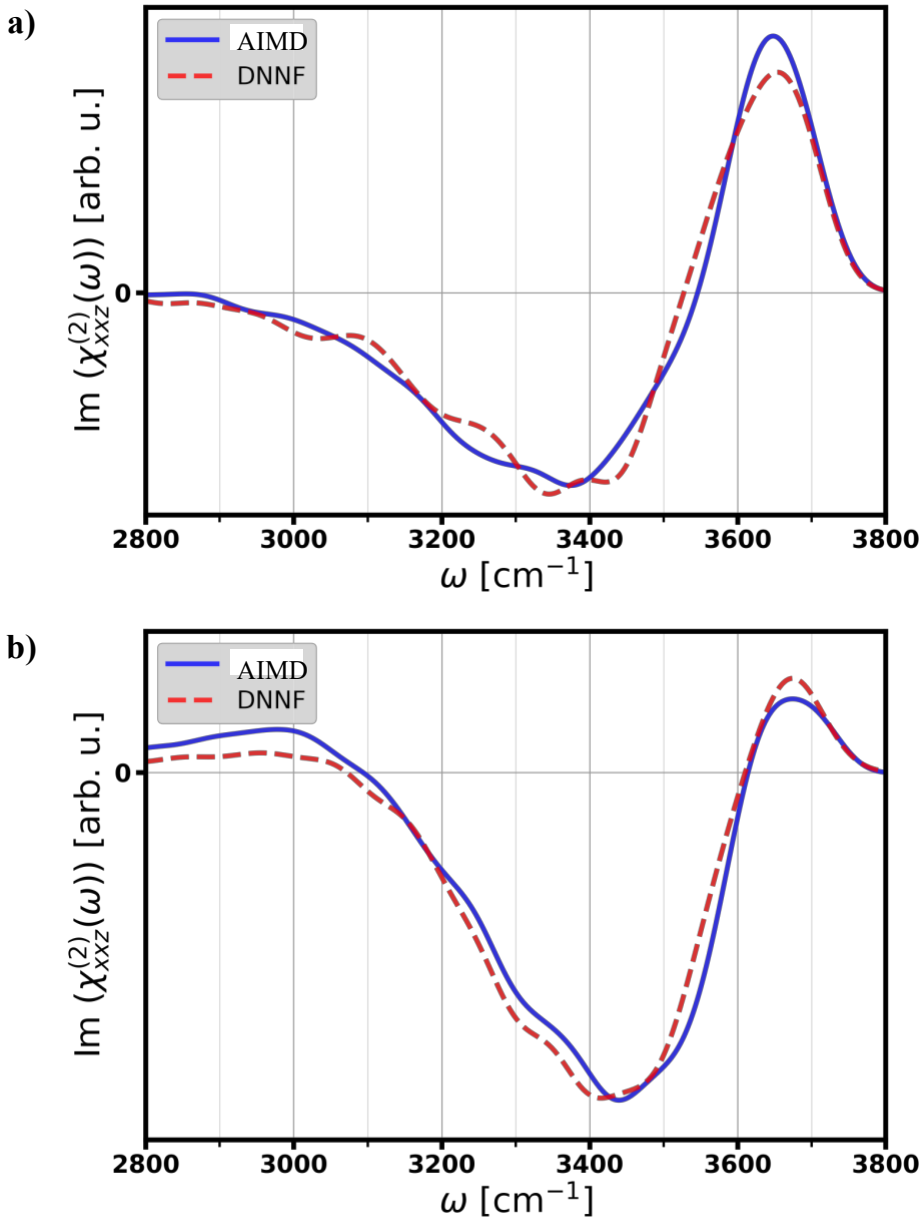

Figure 6. Imaginary part of the simulated vSFG spectra from AIMD and DNNF for a) $GO_{2/1}$-water interface, and b) $GO_{4/1}$-water interface.

The vSFG spectroscopic method is a surface-specific technique that uses χ^2, which is a second-order nonlinear susceptibility that only exists in non-centrosymmetric environments. To gain a more comprehensive understanding of the interface, the resonant imaginary component Im ($\chi^{(2)}_{xxz}$) was analyzed. For the air-water interface, a positive value of Im ($\chi^{(2)}_{xxz}$) denotes a bond with the H atom pointing upward and away from the interface, while a negative value indicates a bond with an OH and H pointing downward and toward the interface.[86] It is worth noting that the exploration of the interface will be from the bottom up, and thus the opposite will hold true in this study. According to the literature, the peak around 3700 cm^{-1} is assigned to dangling OH bonds (free OH) toward the air-water interface[40, 87-90], whereas the peak between 3200-3500 cm^{-1} is attributed to hydrogen-bonded OH bonds pointing away or towards the interface.[40, 87-92] In Figure 6, the imaginary component of vSFG spectra simulated from both AIMD and DNNF is shown. For $GO_{2/1}$-water, both AIMD and DNNF show a positive peak at 3650 cm^{-1} (red-shifted by 50 cm^{-1}) indicating the presence of dangling OH pointing towards the GO-water interface. Both force-fields also exhibit a broad negative peak at 3200-3500 cm^{-1} representing hydrogen-bonded OH pointing away from the interface. For $GO_{4/1}$, DNNF reproduces the smaller positive peak at 3650 cm^{-1} and a broad negative peak at 3200-3500 cm^{-1} although the peak centered for DNNF (3400 cm^{-1}) is slightly red shifted from AIMD (3450 cm^{-1}). The imaginary component of vSFG at the water-air interface for both GO-water systems using DNNF is shown in the supplementary information (Figure S9). DNNF reproduces both peaks (positive 3750 cm^{-1}, negative 3300-3600 cm^{-1}) reported in the literature. DNNF can reproduce vSFG spectra of interfacial water with the same accuracy as AIMD (DFT level).

iv. Hydrogen bond classes

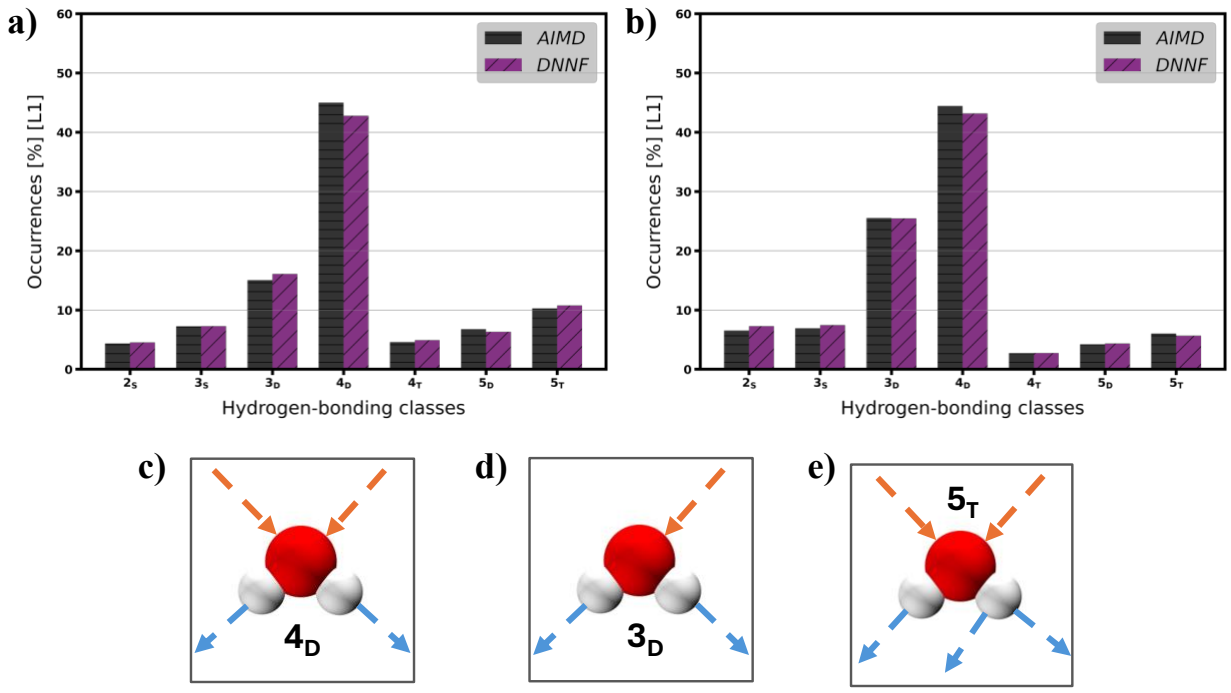

Figure 7. Percentage of different hydrogen bonding classes of L1 water using AIMD and DNNF for a) $GO_{2/1}$, b) $GO_{4/1}$. Representations of hydrogen bonding classes c) 4_D, d) 3_D, e) 5_T. Water oxygens and hydrogens are represented with red and white colors respectively.

The hydrogen bonding environment for both GO-water interfaces was investigated using both AIMD and DNNF. Based on the findings presented in Figure 7, it can be concluded that the most frequently occurring hydrogen bonds in both $GO_{2/1}$ and $GO_{4/1}$ scenarios are double donors as is the case for bulk water. In the case of $GO_{2/1}$, the 4_D class of hydrogen bonds comprises the largest proportion, accounting for 45% in AIMD and 43% in DNNF, with a difference of only 2% in occurrence. The second most common class of hydrogen bonds in $GO_{2/1}$ is 3_D, accounting for 16% in DNNF and 15% in AIMD. Similarly, in $GO_{4/1}$, the 4_D class is also the most prevalent, with around 44% for AIMD and 43% for DNNF. The second most common class of hydrogen bonds in $GO_{4/1}$ is also 3_D, accounting for around 25.5 % for both DNNF and AIMD. The additional hydrogen bond classes were also reproduced for both $GO_{2/1}$ and $GO_{4/1}$. Overall, the results suggest

that DNNF is highly accurate in replicating AIMD hydrogen bond classes. A more detailed explanation of each hydrogen bonding class (including orientation, connection to vSFG spectra and hydrogen bond strength) can be found in previous work by David *et al*.[47]

v. Flexibility of GO sheet

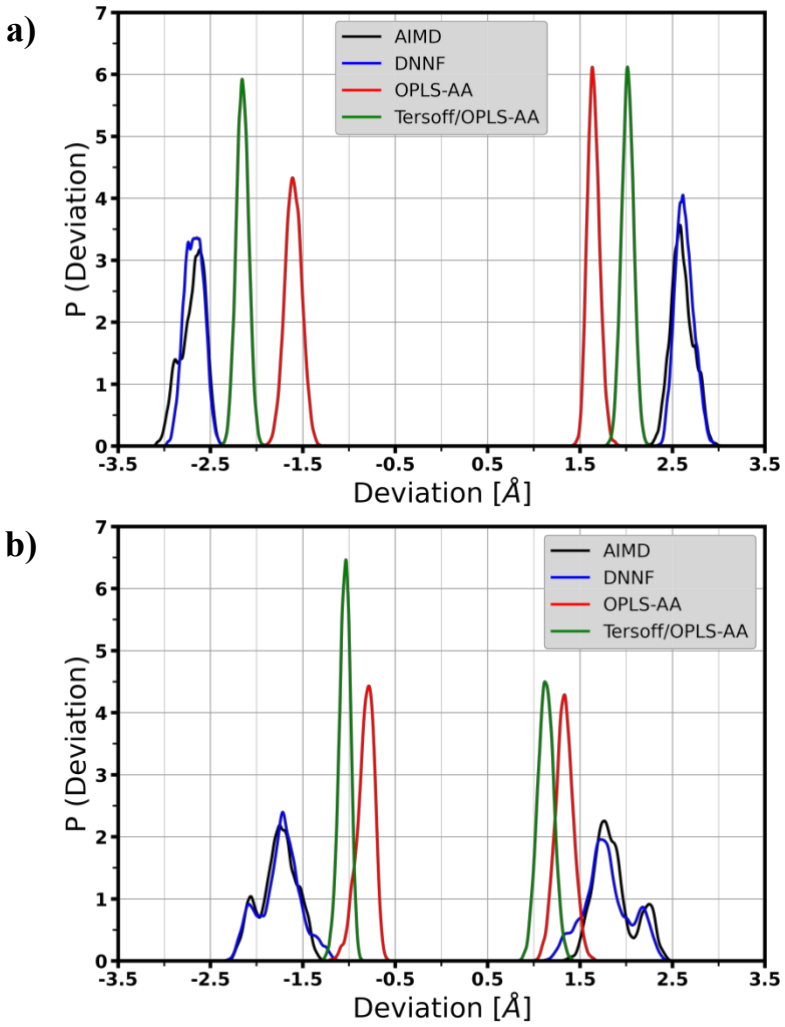

Figure 8. Probability density distribution of maximum displacement in the z-direction of GO carbon atoms. Displacement relative to the average GO surface a) $GO_{2/1}$, b) $GO_{4/1}$. Note that the interface with water is in the positive z-direction.

The incorporation of oxygenated functional groups into GO allows for the formation of a buckled structure, which is not static and the amount of buckling at a given site fluctuates.

Therefore, when modeling GO materials, it is crucial to consider the sheet's flexibility. To examine this, the maximum displacement in both positive and negative directions of the carbon and oxygen atoms in the sheet relative to the average z position of the GO sheet's carbon as a function of time was computed. Based on Figure 8, it appears that $GO_{2/1}$ has a higher maximum deviation in both directions in the case of AIMD. DNNF reproduces this deviation, while Tersoff/OPLS-AA and OPLS-AA have lower deviations than AIMD and DNNF. Similarly, for $GO_{4/1}$, AIMD, and DNNF have the highest maximum deviation in both positive and negative directions compared to OPLS-AA and Tersoff/OPLS-AA. DNNF reproduces the buckling of AIMD for the most part. Furthermore, the distribution of the deviations is highest for the AIMD and DNNF whereas the other force-fields show narrower distributions. The deviation of oxygen atoms follows the same trend as carbons (Figure S10). Both sheets show reactive events, discussed in greater detail later on, in which the epoxy groups can convert to an alcohol group with the erstwhile alcohol group converting to an epoxy group. Thus, not only are the sheets more flexible in the AIMD/DNNF case compared to conventional force-fields, but the reactive events also cause the buckling sites to change in time.

vi. Proton hopping at GO interface

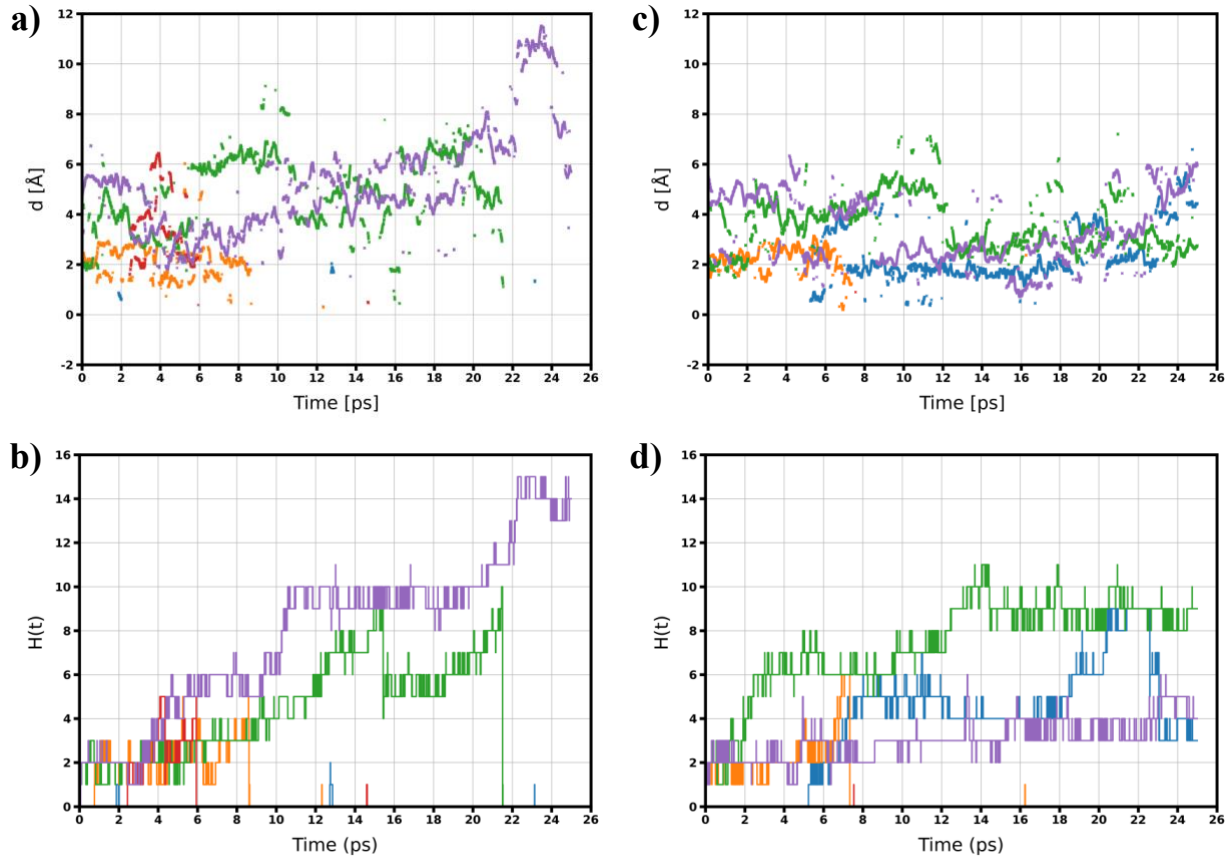

Figure 9. Distance between the oxygen of the hydronium and instantaneous water surface for a) AIMD, c) DNNF. Hopping function H(t) for the corresponding distance b) AIMD, d) DNNF.

One of the significant reactive events in the case of $GO_{2/1}$ is the formation of a proton and its transfer to other water molecules. Following the formation of a proton (hydronium), its identity changes throughout the simulation length and furthermore the hydrated proton can move away from the interface. This change can be tracked using the function H(t) in conjunction with distance d. An increase in H(t) with a constant d indicates hopping parallel to the interface, while an increase in both H(t) and d suggests hopping perpendicular to the interface and away from it. The non-transient nature of the hydronium formed in AIMD studies is discussed in greater detail by David et al.[47,53] These results highlight the intrinsic reactivity of the GO-water interface and Figure 9 demonstrates the ability of the DNNF to capture reactive events such as proton hopping at the

interface that are seen in AIMD simulations. For five different initial structures, the proton hopping event was observed using both AIMD and DNNF. The behavior of hydronium at a longer timescale will be discussed in a later sub-section.

B. Reactivity, interfacial water structure, spectroscopy: From GO to Graphene

The above results clearly show that the DNNF can capture the interfacial water structure, the hydrogen bonding environment as well as the reactivity of the interfacial surface of the two GO systems $GO_{4/1}$ and $GO_{2/1}$. In addition, the DNNF was able to reproduce the forces of the reduced GO system, $GO_{8/1}$, that was not used in the training set. Furthermore, the DNNF allows for extended simulations of hundreds of picoseconds against merely dozens of picoseconds achievable at the AIMD level. In the following section the DNNF is extended to more reduced GO systems including graphene. The interfacial water structure is examined and compared between the different sheets. The vSFG spectra for the sheets from the DNNF simulations are compared to experimental data and the contributions to the spectral signatures are examined. The formation of hydronium ions and the long-time dynamics of phenomena such as proton hopping are investigated.

a. Effect of oxidation level on the interfacial water using DNNF simulations

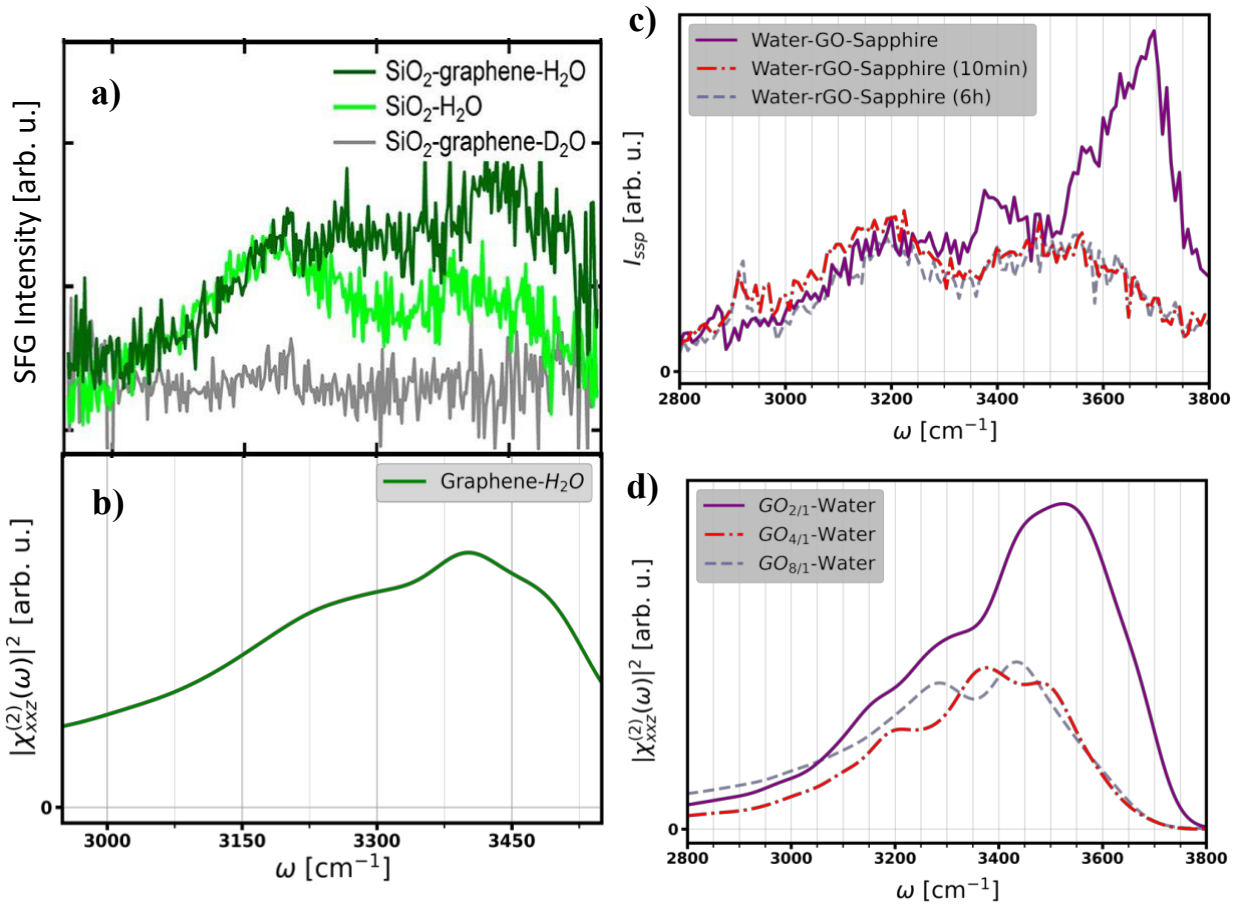

Figure 10. a) Experimental SFG spectra of graphene-water interface when graphene is deposited on SiO_2 substrate.[42] b) Simulated vSFG spectra for graphene-water interface. c) Experimental vSFG spectra of the GO-water interface before and after reduction by SSP polarization. The experiments, reprinted from David *et al.*,[47] were carried out on fully oxidized GO and reduced GO (rGO), reduced for 10 minutes and 6 hours. d) Simulated vSFG spectra of the $GO_{2/1}$-water, $GO_{4/1}$-water, and $GO_{8/1}$-water using the DNNF. The simulated spectra were scaled to have the same height of the maximum as the experiment. (a) is reprinted from Dreier *et al.*[42]

The first set of investigations is on the graphene – water system, the extreme opposite of the fully oxidized $GO_{2/1}$ case. There appears to be some controversy regarding the vSFG spectrum of this system. Investigations on graphene water interfaces both experimentally and computationally have been reported in the literature.[41-43, 48, 93] The water air spectra show a significant spectral peak at 3700 cm^{-1}, which corresponds to dangling OH bond (non-hydrogen-bonded). In a computational study, Ohto *et al*. reported this feature for graphene water interfaces.[48] But from experimental studies, this peak was not observed for a single layer of graphene on a substrate and when the pH is close to 7.[41-43, 94] Two significant peaks at ~3200 cm^{-1} and ~3400 cm^{-1} are observed at graphene water interface from experiments.[42] The peak at ~3200 cm^{-1} is assigned to OH stretching modes of strongly H-bonded water molecules.[95] Nihonyanagi *et al.* found evidence that the ~3400 cm^{-1} peak is associated with relatively weak H-bonded OH group with their H-atoms pointing away from the interface.[40] The relative intensities of this peak vary based on the substrate used in the experiment. When CaF_2 is used as substrate to deposit graphene, a broad peak at ~3200 cm^{-1} is observed.[41, 42] The spectrum for CaF_2 -water interface also gives a similar broad peak at ~3200 cm^{-1}. When SiO_2 is used as substrate, both peaks at ~3200 cm^{-1} and at ~3400 cm^{-1} are observed for the graphene-water interface, where the peak at ~3200 cm^{-1} appears as a shoulder. For the SiO_2-water interface, there is a broad peak at ~3200 cm^{-1} and a shoulder at ~3400 cm^{-1}. These two cases suggest that the substrate can contribute to the spectra. In Figure 10.b, a vSFG spectra is shown for the graphene-water interface using the DNNF. This spectra closely reproduces the experimental SFG spectra of the graphene-water interface when SiO_2 was used as the substrate (Figure 10.a).[42] The simulated spectra has a shoulder at ~3200 cm^{-1} and a peak at ~3400 cm^{-1}.

The vSFG spectra of the fully oxidized and partially reduced GO-water systems from the experimental study[47] and from simulations using the DNNF for GO-water are shown in Figure 10.c and 10.d, respectively. The experimental spectrum of the fully oxidized GO shows a major peak at 3700 cm^{-1} and a broad distribution in the 3000 to 3450 cm^{-1} region with small peaks at around 3200 and 3400 cm^{-1}. After 10 min of reduction the experimental peak at 3700 cm^{-1} disappears, and two broad peaks at 3200 cm^{-1} and 3500 cm^{-1} are observed. When the GO is reduced for 6 hours, there is no significant change in spectral peak compared with reduced GO after 10 mins. The DNNF shows the same trend as the AIMD and the experiment in that there is a significant peak at higher frequencies (red-shifted by around 150 cm^{-1} compared to the experiment) and a broad distribution in the lower frequency region for the fully oxidized case, whereas for the reduced GO cases ($GO_{4/1}$ and $GO_{8/1}$) the high-frequency peak disappears. It should be noted that in this work the intermolecular coupling terms have been neglected in the calculation of the spectra and furthermore additional oxygenated defects, edge defects etc. that are present in the experimental GO sheets have not been included in these simulations. All of these will contribute to the experimental spectrum, making a direct comparison difficult. Nonetheless, the dominant features present in the experimental SFG are well represented in the simulated SFG using DNNF for a wide range of GO-water interfaces, and the graphene-water interface. To further validate the force field, The imaginary component of air-water spectra from all the simulated systems was computed (see Figure S9), which is in agreement with the literature.

b. From highly oxidized GO to graphene: influence on the interfacial water region

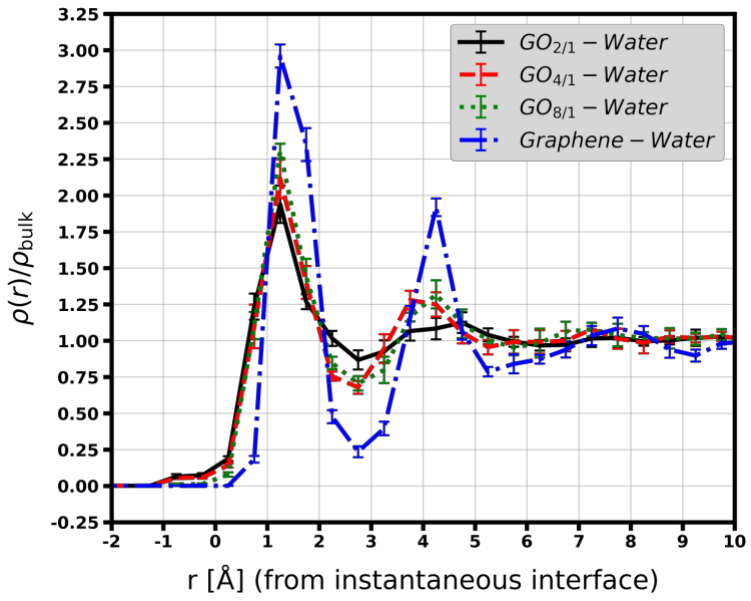

Figure 11. Average water density as a function of distance from instantaneous water interface using DNNF. The simulation trajectory was divided into five blocks and the block averaging method was used to determine the error bars. The error bars represent the standard deviation from the average value.

A comparison of the four different aqueous interfaces, which included $GO_{2/1}$-water, $GO_{4/1}$-water, $GO_{8/1}$-water, and graphene-water with a thick water film (~35 Å) using DNNF is presented. The layering and ordering of water molecules at the interfaces are illustrated in Figure 11. The first minima, also known as the L1 layer, was observed at 2.75 Å for each interface. The first peak for all three GO cases and graphene was observed at 1.25 Å, with the peak intensity showing a notable increase as the GO sheet was progressively reduced, ranging from 1.94 to 2.96. The second water layer (L2) was positioned at 6.25 Å for $GO_{2/1}$, 5.75 Å for $GO_{8/1}$, and 5.25 Å for both $GO_{4/1}$ and Graphene. The peak intensity for the L2 layer varies from 1.12 to 1.92 from $GO_{2/1}$ to Graphene. It was observed that the second water layer (L2) becomes more well-defined as GO is reduced. For graphene, the L2 layer has an intensity similar to the L1 layer of $GO_{2/1}$. In all instances involving

GO, the L3 layer appears like a bulk region, whereas, in the case of graphene, the L3 layer is more structured. This density plot illustrates that water tends to become more ordered and structured as GO is reduced, and the most ordered water layer can be found at the graphene-water interface. As GO is reduced, the water molecules are exposed to the graphene region that has sp^2 carbon-carbon bonds. This graphene region is responsible for the comparatively structured water layer at the GO-water interface.

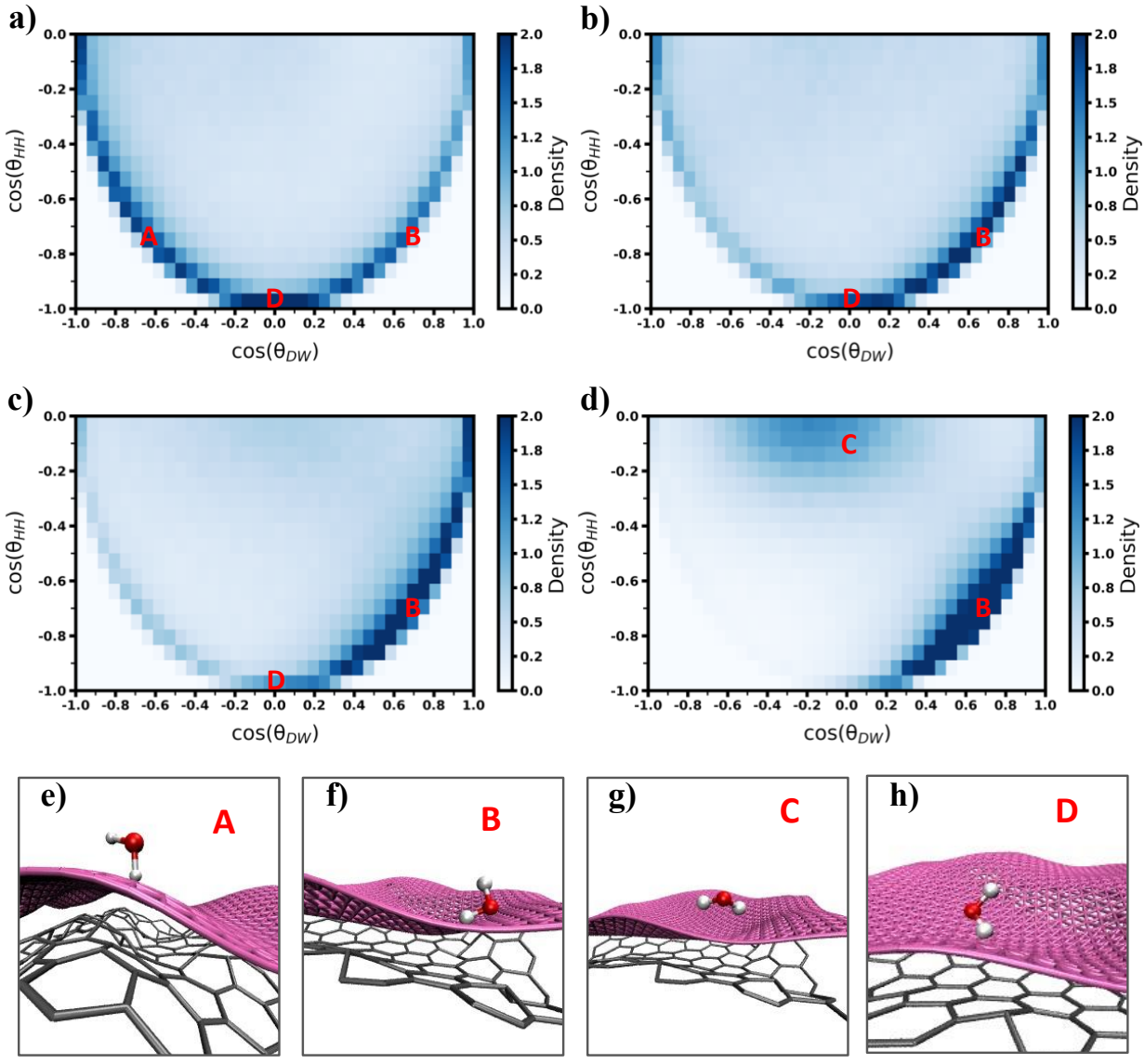

Figure 12. Two-dimensional histogram of joint probability density distribution of $\cos(\theta_{DW})$ and $\cos(\theta_{HH})$ of L1 layer using DNNF for a) $GO_{2/1}$-water, b) $GO_{4/1}$-water, c) $GO_{8/1}$-water, and d) Graphene-water. Representative orientations of water molecules e) $\cos(\theta_{DW})$/$\cos(\theta_{HH})$ pair values equal to -0.71/-0.69 (**A**), f) $\cos(\theta_{DW})$/$\cos(\theta_{HH})$ pair values equal to 0.64/-0.71 (**B**), g) $\cos(\theta_{DW})$/$\cos(\theta_{HH})$ pair values equal to -0.09/-0.09 (**C**), h) $\cos(\theta_{DW})$/$\cos(\theta_{HH})$ pair values equal to 0.03/-0.99 (**D**).

The orientation of water molecules at the L1 layer was investigated by calculating, as before, the two angles θ_{DW} and θ_{HH}. The two-dimensional histogram of joint probability density distribution of $\cos(\theta_{DW})$ and $\cos(\theta_{HH})$ is shown in Figure 12. In the case of $GO_{2/1}$, three major orientational peaks were observed for the orientation of water molecules at the L1 layer. The first peak is in region **B**, where one water OH is pointing away from the interface. The second peak is in region **A**, where one water OH is pointing towards the interface. The third peak is in region **D**, where one water OH is pointing away and another OH is pointing towards the interface. For $GO_{4/1}$, two major peaks in regions **B** and **D** were observed for the orientation of water molecules at the L1 layer. The peak intensity at region **D** decreases compared to $GO_{2/1}$. The $GO_{8/1}$ exhibits a broad major peak in region **B** and a minor peak in region **D**. Graphene also exhibits a broad major peak in region **B** and an intense minor peak in region **C.** As the number of oxygenated functional groups on graphene oxide reduces, the orientational distributions in regions **A** and **D** decrease and finally disappear in the case of graphene. Orientational distributions in regions **B** and **C** increase gradually and become highest in graphene as the number of oxygenated groups reduces. With the reduction in oxidation levels in GO, water OH tends to point away from the interface.

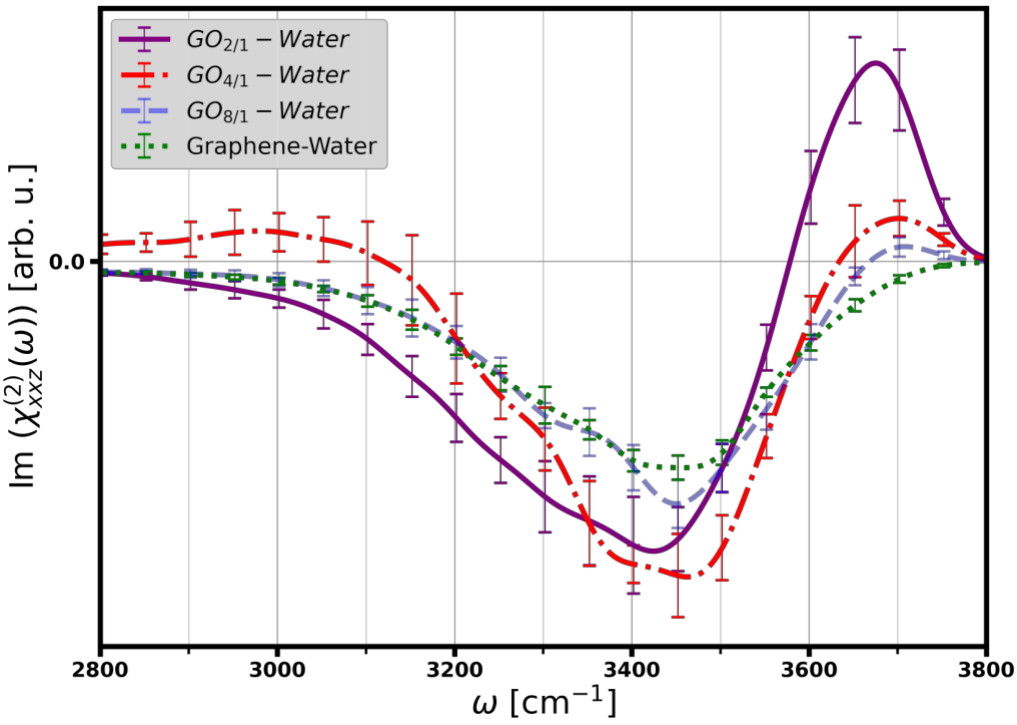

Figure 13. The imaginary part of simulated vSFG spectra for $GO_{2/1}$-water, $GO_{4/1}$-water, $GO_{8/1}$-water, and graphene-water interfaces. The simulation trajectory was divided into five blocks and the block averaging method was used to determine the error bars. The error bars represent the standard deviation from the average value. All spectra were normalized to have unit area.

The orientation of water molecules at the interface is crucial in interpreting the sum frequency generation spectra obtained at the interface. Simulated vSFG spectra were generated using a surface-specific VVCF algorithm, and the imaginary part of the simulated vSFG spectra at the GO-water interface and the graphene-water interface is shown in Figure 13. For $GO_{2/1}$, there is a positive peak at 3670 cm^{-1}, which is the characteristic peak of dangling OH bonds. The positive sign of this peak suggests that the water OH involved was pointing toward the interface. From the observed orientational distribution in Figure 12, two distributions, one with water OH pointing towards the interface (region **A**) and the other with one OH pointing towards the interface

and one pointing away from the interface (region **D**), could be assigned to this peak. There was also a broad negative peak centered at 3420 cm^{-1}, which is characteristic of hydrogen bonded OH. The negative sign of this peak suggests that the OH of water molecules is pointing away from the interface. This peak can be attributed to orientational distributions in regions **B** and **D**. $GO_{4/1}$ has a minor positive peak at 3700 cm^{-1} corresponding to dangling OH bonds. The reduced intensity of this positive peak can be explained by water orientation. For $GO_{4/1}$, the distribution of water orientation, in region **A**, decreases significantly and this peak arises mostly from the distribution in region **D**. There is a broad negative peak centered around the 3450 cm^{-1}, characteristic of H-bonded OH mainly arising from the distribution region **B** and partially from distributions in region **D**. There is also a slight positive peak at ~3000 cm^{-1}. For $GO_{8/1}$ there is a negligible peak at 3700 cm^{-1}. The distribution of orientation in region **D**, decreases significantly, causing a reduced peak intensity. The broad negative peak centered at 3450 cm^{-1} and shoulder at 3300 cm^{-1} solely comes from the distribution in region **B**. For graphene, the positive peak at 3700 cm^{-1} completely disappears as the distribution in region **D** disappears. The broad peak centered around 3450 cm^{-1} solely comes from the distribution where OH of water molecules pointing away from the interface. The region C with waters O-Hs parallel to the interface has negligible contribution to the spectrum.

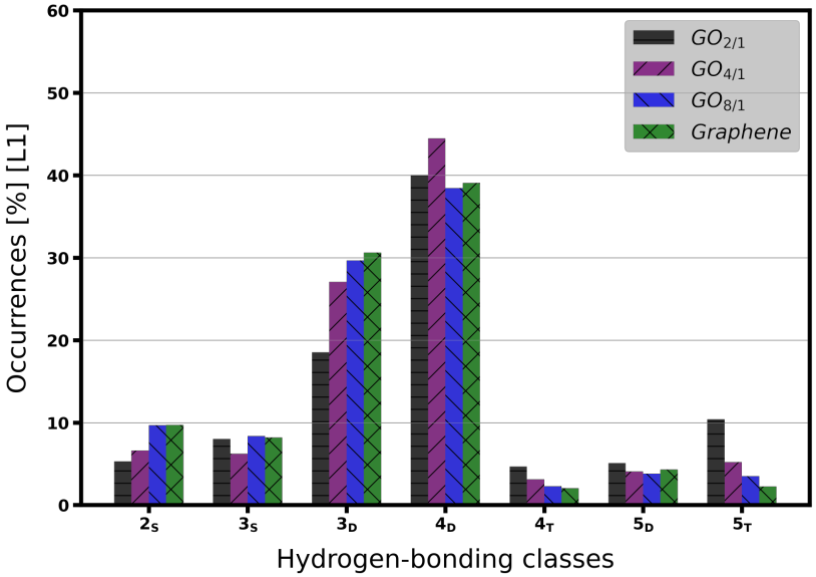

Figure 14. Distribution of different hydrogen bonding classes (N_X) of L1 water for $GO_{2/1}$-water, $GO_{4/1}$-water, $GO_{8/1}$-water, and graphene-water interface, where N is the total number of hydrogen bonds that a water molecule is involved in (both as donor and acceptor) and X refers to the total number of donors (S-single, D- double and T- triple).

The hydrogen bonding environment for all four interfaces is shown in Figure 14. It is observed that the predominant hydrogen-bonding class in each interface is 4_D, in which one water molecule has a total of four hydrogen bonds with a double donor. The second most common class is 3_D, which has a total of three hydrogen bonds with a double donor. In $GO_{2/1}$, the major hydrogen bonding classes are 4_D (40%) and 3_D (18.5%). The 5_D and 5_T classes, which have a higher total number of hydrogen bonds, account for 5% and 10.5%, respectively. Other hydrogen bonding classes such as 2_S, 3_S, and 4_T represent 5.3%, 8%, and 4.7%, respectively. Transitioning to $GO_{4/1}$, the distribution alters slightly, with 4_D, 3_D, 2_S, 3_S, 4_T, 5_D, and 5_T classes accounting for 44.5%, 27%, 6.5%, 6%, 3%, 4%, and 5%, respectively. In $GO_{8/1}$, these proportions shift to 38.5%, 29.5%, 9.5%, 8.5%, 2.2%, 3.7%, and 3.5% for the same classes. Similarly, for graphene, these classes are

composed of 39%, 30.5%, 9.5%, 8.5%, 2%, 4.3% and 2.2%, respectively. It is interesting to notice that the percentage of triple donors (4_T, 5_T) decreases as the functional groups in the GO sheet are reduced. Conversely, hydrogen bonding classes with a lower number of hydrogen bonds (2_S, 3_D) increase with the reduction of functional groups, since these sheets have fewer oxygenated defects to which the interfacial water can hydrogen bond to.

Reactive events are observed only in the GO-water interfaces, while no reactivity was observed at the interface or bulk in the graphene-water simulations. In the case of all three GO interfaces, a common event is the opening of epoxide to form an alkoxide and carbocation pair (Figure S12.a and S12.b). In the case of $GO_{2/1}$, these alkoxides can either react with the same carbocation to close the epoxide or react with nearby alcohol to form an alcohol and another alkoxide. Alternatively, they can remain as an alkoxide in the GO sheet. In $GO_{4/1}$, a reaction can occur between carbocation and the same or different alkoxide, resulting in the formation of a new epoxide. An alcohol and alkoxide pair are formed when an alkoxide reacts with another nearby alcohol. Long-lived carbocations are more prevalent in $GO_{4/1}$ compared to $GO_{2/1}$. In $GO_{8/1}$, an epoxide can be formed by the reaction between an alkoxide and carbocation, or it can form an alcohol by getting protonated from hydronium or nearby alcohol. One stabilized carbocation remains in the GO sheet. The simulation also includes the formation of new species. In the case of $GO_{2/1}$, the formation of ketone (Figure S12.e and S12.f) from epoxide is significant and can occur in two ways: the epoxide ring opens, and a double bond is created between carbon and oxygen, or the alkoxide becomes a ketone by forming a double bond between carbon and oxygen and making a nearby carbocation. The formation of ketone in $GO_{4/1}$ and $GO_{8/1}$ is not significant compared to $GO_{2/1}$. Formation of ether (Figure S12.c and S12.d) by breaking C-C bonds was also observed mainly in the $GO_{4/1}$ case. The formation of ether is not significant for $GO_{2/1}$ and $GO_{8/1}$. One reactive

event that occurs significantly in all three interfaces with the same intensity is the interchange between alkoxide and alcohol. Although rare, the formation of protonated alcohol is observed in the case of $GO_{2/1}$ and $GO_{4/1,}$ which can be a precursor of forming water and leaving the GO sheet making a carbocation[53] as reported in the literature. Formation of protonated epoxy is observed in the case of $GO_{2/1}$ and $GO_{8/1,}$ but it is absent in $GO_{4/1,}$ where alcohol oxygen connects with a carbocation. The reverse reaction also occurs to form alcohol and carbocation. In the case of $GO_{8/1}$, protonated epoxide gives its proton to water, resulting in a hydronium ion. The formation of long-lived hydronium and its Grotthuss transport[50] in aqueous solution are the most interesting events for $GO_{2/1}$. Hydronium is formed when an alcohol at the edge protonates a nearby water and makes an alkoxide along with it. This results in the aqueous media becoming acidic. In the DNNF trajectory, a hydronium ion forms at the GO-water interface during equilibration and then hops forward to approximately 33 Å from the instantaneous surface (Figure 15) towards the air-water interface. The propensity of hydronium to move at the air-water interface is reported both experimentally and in simulations.[50, 52, 96] After almost 100 ps, another hydronium forms at the GO-water interface where an alcohol at the edge of the GO sheet protonates another water by becoming an alkoxide. This proton then moves forward but doesn't move far away, staying near the GO-water interface. After 200 ps, both protons stay near the GO-water interface. After that, one of the protons hops and moves a little away from the GO-water interfaces, while the other one hops parallel to the interface and stays near the interface till 300 ps. Beyond the 300 ps shown in Figure 15, other hydronium formations and proton hopping events involving the sheet itself are seen and are briefly outlined here. After around 400 ps, one hydronium loses a proton by transferring it to an alkoxide on the GO sheet, resulting in the formation of an alcohol and water. At around 500 ps, another hydronium forms when another alcohol is deprotonated by transferring

its proton to a water, and then both protons hop to other waters. Relevant snapshots depicting the formation and migration of the hydronium ion are shown in Figure S11. This analysis of the trajectories shows that multiple hydronium formation events occur, and the acidic proton once formed can hop between water molecules. Interestingly, the experimental work of Dimiev et al. indicates that the water near the fully oxidized GO surface is acidic and determines the resulting pKa of the GO system.[97] In the case of $GO_{4/1}$ and $GO_{8/1}$, transient hydronium ions can form, which have a lifetime of less than 1 ps.

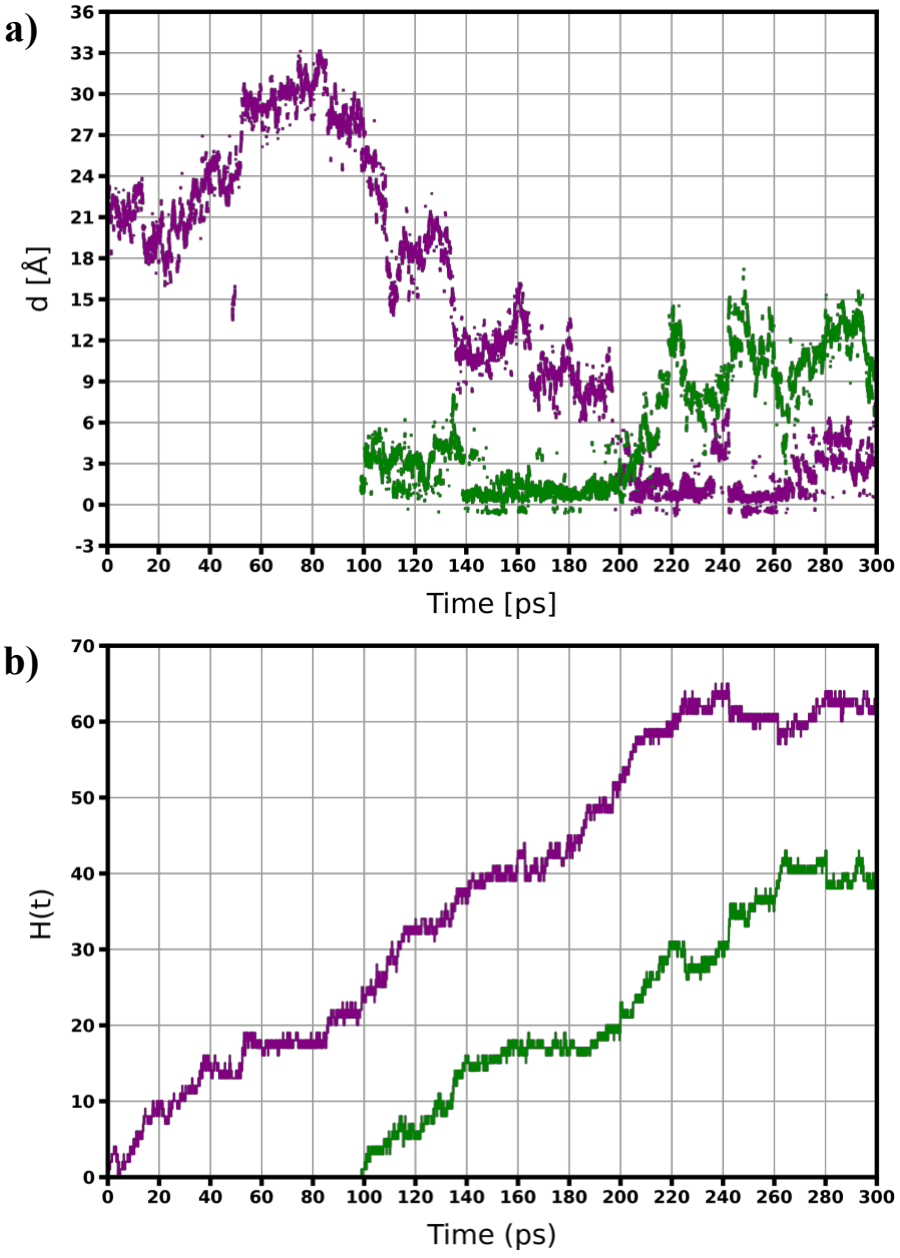

Figure 15. a) Distance of hydronium from the instantaneous interface over 300 ps. b) Corresponding hydronium hopping function H(t). The purple color represents the formation of hydronium at the beginning of the simulation and the green color represents the formation of another concurrent hydronium in the same simulation.

IV. Conclusions

The aqueous interface with graphene and with graphene oxides at varying oxidation levels was examined from simulations using a neural network force-field. The neural network force field was developed for graphene oxide-water that gives *ab-initio* accuracy while being ~18000 times faster. Although this forcefield was developed based on two oxidation levels of GO-water data, it was validated on $GO_{8/1}$ and the graphene-water interfaces, which makes it transferrable to other oxidation levels of the GO system. The forcefield is also effective across various temperatures. The vSFG spectrum of GO-water at different oxidation levels and the graphene-water system were examined and compared. Interestingly, the simulation was able to reproduce the experimental vSFG spectra which are clearly correlated to the specific orientations of the interfacial waters. The DNNF force field revealed hydronium formation and long-lived hydronium species as well as proton hopping events. Furthermore, since the simulation times are much longer, by at least an order of magnitude compared to what is achievable using AIMD, it enabled the investigation of multiple hydronium ion formation events along with proton hopping, including proton transport to the air-water interface and back again to the GO interface. This suggests that the interfacial water in these oxidized GO systems is acidic. The vibrational sum frequency generation spectra were calculated for the different graphene-based interfaces and shown to reproduce experimental spectral signatures. The latter were connected to the interfacial water structure and orientation. As the GO sheet is reduced the high frequency component of the spectra decreases. Furthermore, the DNNF simulations also revealed the significant structuring of the interfacial waters along with a decrease in reactive events as the sheet is reduced. The buckling of the GO sheet arises due to the presence of oxygenated functional groups, which in turn introduces strain within the GO sheet, leading to the formation of various new species. In contrast, graphene sheets remain planar and

show no reactive events during the DNNF simulations. In summary, DNNF based simulations have led to the exploration of graphene oxide (GO) reactivity beyond the capabilities of AIMD. This work also underscores the transferability of DNNFFs across different temperatures and oxidation levels, validated through comparisons with both AIMD and experimental vSFG data. These investigations pave the way for further, more targeted studies on the reactivity of graphene oxide-liquid interfaces.

ACKNOWLEDGMENTS

This work was supported by the National Science Foundation, grant number CHE-1845795. The simulations were carried out at the LSU-HPC and LONI facilities.

Supporting Information

The details of the simulation setup, force prediction graphs for the DNNF, comparison of the various radial distribution functions between AIMD and DNNF, difference plot of the angle distribution between AIMD and DNNF and AIMD and different force-fields, air-water VSFG spectra, O atom fluctuations in the sheet, and snapshots of hydronium formation and deprotonation events are included. The DNNF force-field is available at https://github.com/KumarGroupLSU/dnnf_go.

References

(1) Su, C.; Acik, M.; Takai, K.; Lu, J.; Hao, S. J.; Zheng, Y.; Wu, P.; Bao, Q.; Enoki, T.; Chabal, Y. J.; Loh, K. P. Probing the catalytic activity of porous graphene oxide and the origin of this behaviour. *Nat Commun* **2012**, *3*, 1298.
(2) Navalon, S.; Dhakshinamoorthy, A.; Alvaro, M.; Garcia, H. Carbocatalysis by graphene-based materials. *Chem Rev* **2014**, *114* (12), 6179-6212.
(3) Dhakshinamoorthy, A.; Alvaro, M.; Concepcion, P.; Fornes, V.; Garcia, H. Graphene oxide as an acid catalyst for the room temperature ring opening of epoxides. *Chem Commun (Camb)* **2012**, *48* (44), 5443-5445.
(4) Chen, Y.; Luo, Z.; Lu, X. Construction of Novel Enzyme-Graphene Oxide Catalytic Interface with Improved Enzymatic Performance and Its Assembly Mechanism. *ACS Appl Mater Interfaces* **2019**, *11* (12), 11349-11359.
(5) Kim, D.; Kim, D. W.; Lim, H.-K.; Jeon, J.; Kim, H.; Jung, H.-T.; Lee, H. Intercalation of Gas Molecules in Graphene Oxide Interlayer: The Role of Water. *The Journal of Physical Chemistry C* **2014**, *118* (20), 11142-11148.
(6) Zhao, G.; Jiang, L.; He, Y.; Li, J.; Dong, H.; Wang, X.; Hu, W. Sulfonated graphene for persistent aromatic pollutant management. *Adv Mater* **2011**, *23* (34), 3959-3963.
(7) Madadrang, C. J.; Kim, H. Y.; Gao, G.; Wang, N.; Zhu, J.; Feng, H.; Gorring, M.; Kasner, M. L.; Hou, S. Adsorption behavior of EDTA-graphene oxide for Pb (II) removal. *ACS Appl Mater Interfaces* **2012**, *4* (3), 1186-1193.
(8) Liu, F.; Chung, S.; Oh, G.; Seo, T. S. Three-dimensional graphene oxide nanostructure for fast and efficient water-soluble dye removal. *ACS Appl Mater Interfaces* **2012**, *4* (2), 922-927.
(9) Romanchuk, A. Y.; Slesarev, A. S.; Kalmykov, S. N.; Kosynkin, D. V.; Tour, J. M. Graphene oxide for effective radionuclide removal. *Phys Chem Chem Phys* **2013**, *15* (7), 2321-2327.
(10) Wang, J.; Chen, B. Adsorption and coadsorption of organic pollutants and a heavy metal by graphene oxide and reduced graphene materials. *Chem. Eng. J.* **2015**, *281*, 379-388.
(11) Guo, H.; Jiao, T.; Zhang, Q.; Guo, W.; Peng, Q.; Yan, X. Preparation of Graphene Oxide-Based Hydrogels as Efficient Dye Adsorbents for Wastewater Treatment. *Nanoscale Res Lett* **2015**, *10* (1), 931.
(12) Xu, Q.; Xu, H.; Chen, J.; Lv, Y.; Dong, C.; Sreeprasad, T. S. Graphene and graphene oxide: advanced membranes for gas separation and water purification. *Inorganic Chemistry Frontiers* **2015**, *2* (5), 417-424, 10.1039/C4QI00230J.
(13) Hegab, H. M.; Zou, L. Graphene oxide-assisted membranes: Fabrication and potential applications in desalination and water purification. *Journal of Membrane Science* **2015**, *484*, 95-106.
(14) Thakur, K.; Kandasubramanian, B. Graphene and Graphene Oxide-Based Composites for Removal of Organic Pollutants: A Review. *Journal of Chemical & Engineering Data* **2019**, *64* (3), 833-867.
(15) Subasinghege Don, V.; Kim, L.; David, R.; Nauman, J. A.; Kumar, R. Adsorption Studies at the Graphene Oxide–Liquid Interface: A Molecular Dynamics Study. *The Journal of Physical Chemistry C* **2023**, *127* (12), 5920-5930.

(16) Carr, A. J.; Lee, S. E.; Kumal, R. R.; Bu, W.; Uysal, A. Convenient Confinement: Interplay of Solution Conditions and Graphene Oxide Film Structure on Rare Earth Separations. *ACS Appl Mater Interfaces* **2022**, *14* (51), 57133-57143.
(17) Kumal, R. R.; Carr, A. J.; Uysal, A. **2022**.
(18) Carr, A. J.; Kumal, R. R.; Bu, W.; Uysal, A. Effects of ion adsorption on graphene oxide films and interfacial water structure: A molecular-scale description. *Carbon* **2022**, *195*, 131-140.
(19) Chen, D.; Feng, H.; Li, J. Graphene oxide: preparation, functionalization, and electrochemical applications. *Chem Rev* **2012**, *112* (11), 6027-6053.
(20) DeYoung, A. D.; Park, S.-W.; Dhumal, N. R.; Shim, Y.; Jung, Y.; Kim, H. J. Graphene Oxide Supercapacitors: A Computer Simulation Study. *The Journal of Physical Chemistry C* **2014**, *118* (32), 18472-18480.
(21) Ban, S.; Jing, X.; Zhou, H.; Zhang, L.; Zhang, J. Experimental and modeling study on charge storage/transfer mechanism of graphene-based supercapacitors. *J. Power Sources* **2014**, *268*, 604-609.
(22) Martins, M. V.; Pereira, A. R.; Luz, R. A.; Iost, R. M.; Crespilho, F. N. Evidence of short-range electron transfer of a redox enzyme on graphene oxide electrodes. *Phys Chem Chem Phys* **2014**, *16* (33), 17426-17436.
(23) Gao, W.; Wu, G.; Janicke, M. T.; Cullen, D. A.; Mukundan, R.; Baldwin, J. K.; Brosha, E. L.; Galande, C.; Ajayan, P. M.; More, K. L.; et al. Ozonated graphene oxide film as a proton-exchange membrane. *Angew Chem Int Ed Engl* **2014**, *53* (14), 3588-3593.
(24) Lee, O.-S.; Carignano, M. A. Exfoliation of Electrolyte-Intercalated Graphene: Molecular Dynamics Simulation Study. *The Journal of Physical Chemistry C* **2015**, *119* (33), 19415-19422.
(25) Pandey, R. P.; Shukla, G.; Manohar, M.; Shahi, V. K. Graphene oxide based nanohybrid proton exchange membranes for fuel cell applications: An overview. *Adv Colloid Interface Sci* **2017**, *240*, 15-30.
(26) Hu, B.; Hu, Q.; Li, X.; Pan, H.; Tang, X.; Chen, C.; Huang, C. Rapid and highly efficient removal of Eu(III) from aqueous solutions using graphene oxide. *Journal of Molecular Liquids* **2017**, *229*, 6-14.
(27) Xie, Y.; Helvenston, E. M.; Shuller-Nickles, L. C.; Powell, B. A. Surface Complexation Modeling of Eu(III) and U(VI) Interactions with Graphene Oxide. *Environ Sci Technol* **2016**, *50* (4), 1821-1827.
(28) Xie, Y.; Powell, B. A. Linear Free Energy Relationship for Actinide Sorption to Graphene Oxide. *ACS Appl Mater Interfaces* **2018**, *10* (38), 32086-32092.
(29) Bliznyuk, V. N.; Conroy, N. A.; Xie, Y.; Podila, R.; Rao, A. M.; Powell, B. A. Increase in the reduction potential of uranyl upon interaction with graphene oxide surfaces. *Phys Chem Chem Phys* **2018**, *20* (3), 1752-1760.
(30) Romaniak, G.; Dybowski, K.; Jeziorna, A.; Kula, P.; Kaźmierczak, T. Synthesis and characterization of semi-permeable graphene/graphene oxide membranes for water desalination. *Journal of Materials Science* **2020**, *55* (23), 9775-9786.
(31) Shih, C. J.; Lin, S.; Sharma, R.; Strano, M. S.; Blankschtein, D. Understanding the pH-dependent behavior of graphene oxide aqueous solutions: a comparative experimental and molecular dynamics simulation study. *Langmuir* **2012**, *28* (1), 235-241.
(32) Garg, B.; Bisht, T.; Ling, Y. C. Graphene-based nanomaterials as heterogeneous acid catalysts: a comprehensive perspective. *Molecules* **2014**, *19* (9), 14582-14614.

(33) Sun, Y.; Yang, S.; Chen, Y.; Ding, C.; Cheng, W.; Wang, X. Adsorption and desorption of U(VI) on functionalized graphene oxides: a combined experimental and theoretical study. *Environ Sci Technol* **2015**, *49* (7), 4255-4262.
(34) Tan, L.; Wang, S.; Du, W.; Hu, T. Effect of water chemistries on adsorption of Cs(I) onto graphene oxide investigated by batch and modeling techniques. *Chemical Engineering Journal* **2016**, *292*, 92-97.
(35) Carr, A. J.; Lee, S. S.; Uysal, A. Trivalent ion overcharging on electrified graphene. *J Phys Condens Matter* **2022**, *34* (14).
(36) Bonn, M.; Nagata, Y.; Backus, E. H. Molecular structure and dynamics of water at the water-air interface studied with surface-specific vibrational spectroscopy. *Angew Chem Int Ed Engl* **2015**, *54* (19), 5560-5576.
(37) Carr, A. J.; Lee, S. E.; Uysal, A. Ion and water adsorption to graphene and graphene oxide surfaces. *Nanoscale* **2023**, *15* (35), 14319-14337.
(38) Bonatout, N.; Muller, F.; Fontaine, P.; Gascon, I.; Konovalov, O.; Goldmann, M. How exfoliated graphene oxide nanosheets organize at the water interface: evidence for a spontaneous bilayer self-assembly. *Nanoscale* **2017**, *9* (34), 12543-12548.
(39) Stiopkin, I. V.; Jayathilake, H. D.; Bordenyuk, A. N.; Benderskii, A. V. Heterodyne-detected vibrational sum frequency generation spectroscopy. *J Am Chem Soc* **2008**, *130* (7), 2271-2275.
(40) Nihonyanagi, S.; Yamaguchi, S.; Tahara, T. Direct evidence for orientational flip-flop of water molecules at charged interfaces: a heterodyne-detected vibrational sum frequency generation study. *J Chem Phys* **2009**, *130* (20), 204704.
(41) Kim, D.; Kim, E.; Park, S.; Kim, S.; Min, B. K.; Yoon, H. J.; Kwak, K.; Cho, M. Wettability of graphene and interfacial water structure. *Chem* **2021**, *7* (6), 1602-1614.
(42) Dreier, L. B.; Liu, Z.; Narita, A.; van Zadel, M. J.; Mullen, K.; Tielrooij, K. J.; Backus, E. H. G.; Bonn, M. Surface-Specific Spectroscopy of Water at a Potentiostatically Controlled Supported Graphene Monolayer. *J Phys Chem C Nanomater Interfaces* **2019**, *123* (39), 24031-24038.
(43) Singla, S.; Anim-Danso, E.; Islam, A. E.; Ngo, Y.; Kim, S. S.; Naik, R. R.; Dhinojwala, A. Insight on Structure of Water and Ice Next to Graphene Using Surface-Sensitive Spectroscopy. *ACS Nano* **2017**, *11* (5), 4899-4906.
(44) Nagata, Y.; Hsieh, C. S.; Hasegawa, T.; Voll, J.; Backus, E. H.; Bonn, M. Water Bending Mode at the Water-Vapor Interface Probed by Sum-Frequency Generation Spectroscopy: A Combined Molecular Dynamics Simulation and Experimental Study. *J Phys Chem Lett* **2013**, *4* (11), 1872-1877.
(45) Auer, B. M.; Skinner, J. L. Vibrational sum-frequency spectroscopy of the liquid/vapor interface for dilute HOD in D(2)O. *J Chem Phys* **2008**, *129* (21), 214705.
(46) Kishinaka, S.; Morita, A.; Ishiyama, T. Molecular structure and vibrational spectra at water/poly(2-methoxyethylacrylate) and water/poly(methyl methacrylate) interfaces: A molecular dynamics simulation study. *J Chem Phys* **2019**, *150* (4), 044707.
(47) David, R.; Tuladhar, A.; Zhang, L.; Arges, C.; Kumar, R. Effect of Oxidation Level on the Interfacial Water at the Graphene Oxide-Water Interface: From Spectroscopic Signatures to Hydrogen-Bonding Environment. *J Phys Chem B* **2020**, *124* (37), 8167-8178.
(48) Ohto, T.; Tada, H.; Nagata, Y. Structure and dynamics of water at water-graphene and water-hexagonal boron-nitride sheet interfaces revealed by ab initio sum-frequency generation spectroscopy. *Phys Chem Chem Phys* **2018**, *20* (18), 12979-12985.

(49) Zhang, X.; Arges, C.; Kumar, R. Computational Investigations of the Water Structure at α-Al2O3(0001)-Water Interfaces. **2023**.
(50) Kumar, R.; Knight, C.; Voth, G. A. Exploring the behaviour of the hydrated excess proton at hydrophobic interfaces. *Faraday Discuss* **2013**, *167*, 263-278.
(51) Giberti, F.; Hassanali, A. A. The excess proton at the air-water interface: The role of instantaneous liquid interfaces. *J Chem Phys* **2017**, *146* (24), 244703.
(52) Buch, V.; Milet, A.; Vacha, R.; Jungwirth, P.; Devlin, J. P. Water surface is acidic. *Proc Natl Acad Sci U S A* **2007**, *104* (18), 7342-7347.
(53) David, R.; Kumar, R. Reactive events at the graphene oxide-water interface. *Chem Commun (Camb)* **2021**, *57* (88), 11697-11700.
(54) Car, R.; Parrinello, M. Unified approach for molecular dynamics and density-functional theory. *Phys Rev Lett* **1985**, *55* (22), 2471-2474.
(55) Behler, J. First Principles Neural Network Potentials for Reactive Simulations of Large Molecular and Condensed Systems. *Angew Chem Int Ed Engl* **2017**, *56* (42), 12828-12840.
(56) Deringer, V. L.; Caro, M. A.; Csanyi, G. Machine Learning Interatomic Potentials as Emerging Tools for Materials Science. *Adv Mater* **2019**, *31* (46), e1902765.
(57) Bartok, A. P.; Payne, M. C.; Kondor, R.; Csanyi, G. Gaussian approximation potentials: the accuracy of quantum mechanics, without the electrons. *Phys Rev Lett* **2010**, *104* (13), 136403.
(58) Chmiela, S.; Tkatchenko, A.; Sauceda, H. E.; Poltavsky, I.; Schutt, K. T.; Muller, K. R. Machine learning of accurate energy-conserving molecular force fields. *Sci Adv* **2017**, *3* (5), e1603015.
(59) Behler, J. Constructing high‐dimensional neural network potentials: A tutorial review. *International Journal of Quantum Chemistry* **2015**, *115* (16), 1032-1050.
(60) Behler, J.; Parrinello, M. Generalized neural-network representation of high-dimensional potential-energy surfaces. *Phys Rev Lett* **2007**, *98* (14), 146401.
(61) Wang, H.; Zhang, L.; Han, J.; E, W. DeePMD-kit: A deep learning package for many-body potential energy representation and molecular dynamics. *Computer Physics Communications* **2018**, *228*, 178-184.
(62) Han, J.; Zhang, L.; Car, R.; E, W. Deep Potential: A General Representation of a Many-Body Potential Energy Surface. *Communications in Computational Physics* **2018**, *23* (3).
(63) Zhang, L.; Han, J.; Wang, H.; Wissam; Car, R.; E, W. End-to-end Symmetry Preserving Inter-atomic Potential Energy Model for Finite and Extended Systems. *arXiv pre-print server* **2018**.
(64) Batzner, S.; Musaelian, A.; Sun, L.; Geiger, M.; Mailoa, J. P.; Kornbluth, M.; Molinari, N.; Smidt, T. E.; Kozinsky, B. E(3)-equivariant graph neural networks for data-efficient and accurate interatomic potentials. *Nat Commun* **2022**, *13* (1), 2453.
(65) Zeng, J.; Zhang, D.; Lu, D.; Mo, P.; Li, Z.; Chen, Y.; Rynik, M.; Huang, L.; Li, Z.; Shi, S.; et al. DeePMD-kit v2: A software package for deep potential models. *J Chem Phys* **2023**, *159* (5).
(66) Zhuang, Y. B.; Bi, R. H.; Cheng, J. Resolving the odd-even oscillation of water dissociation at rutile TiO(2)(110)-water interface by machine learning accelerated molecular dynamics. *J Chem Phys* **2022**, *157* (16), 164701.
(67) Zeng, Z.; Wodaczek, F.; Liu, K.; Stein, F.; Hutter, J.; Chen, J.; Cheng, B. Mechanistic insight on water dissociation on pristine low-index TiO(2) surfaces from machine learning molecular dynamics simulations. *Nat Commun* **2023**, *14* (1), 6131.
(68) Lai, G.; Jiao, J.; Fang, C.; Zhang, R.; Xu, X.; Sheng, L.; Jiang, Y.; Ouyang, C.; Zheng, J. A Deep Neural Network Interface Potential for Li‐Cu Systems. *Advanced Materials Interfaces* **2022**, *9* (27).

(69) Zhao, W.; Qiu, H.; Guo, W. A Deep Neural Network Potential for Water Confined in Graphene Nanocapillaries. *The Journal of Physical Chemistry C* **2022**, *126* (25), 10546-10553.
(70) de la Puente, M.; David, R.; Gomez, A.; Laage, D. Acids at the Edge: Why Nitric and Formic Acid Dissociations at Air-Water Interfaces Depend on Depth and on Interface Specific Area. *J Am Chem Soc* **2022**, *144* (23), 10524-10529.
(71) Galib, M.; Limmer, D. T. Reactive uptake of N(2)O(5) by atmospheric aerosol is dominated by interfacial processes. *Science* **2021**, *371* (6532), 921-925.
(72) de la Puente, M.; Laage, D. How the Acidity of Water Droplets and Films Is Controlled by the Air-Water Interface. *J Am Chem Soc* **2023**, *145* (46), 25186-25194.
(73) Yang, M.; Bonati, L.; Polino, D.; Parrinello, M. Using metadynamics to build neural network potentials for reactive events: the case of urea decomposition in water. *Catalysis Today* **2022**, *387*, 143-149.
(74) Devergne, T.; Magrino, T.; Pietrucci, F.; Saitta, A. M. Combining Machine Learning Approaches and Accurate Ab Initio Enhanced Sampling Methods for Prebiotic Chemical Reactions in Solution. *J Chem Theory Comput* **2022**, *18* (9), 5410-5421.
(75) Benayad, Z.; David, R.; Stirnemann, G. Molecular mechanisms of phosphoester bond formation in abiotic conditions with reactive neural network potentials. *ChemRxiv. 2023* **2023**.
(76) Willard, A. P.; Chandler, D. Instantaneous liquid interfaces. *J Phys Chem B* **2010**, *114* (5), 1954-1958.
(77) Pezzotti, S.; Galimberti, D. R.; Gaigeot, M. P. 2D H-Bond Network as the Topmost Skin to the Air-Water Interface. *J Phys Chem Lett* **2017**, *8* (13), 3133-3141.
(78) Kumar, R.; Schmidt, J. R.; Skinner, J. L. Hydrogen bonding definitions and dynamics in liquid water. *J Chem Phys* **2007**, *126* (20), 204107.
(79) Mountain, R. D. Molecular dynamics investigation of expanded water at elevated temperatures. *The Journal of Chemical Physics* **1989**, *90* (3), 1866-1870.
(80) Sato, H.; Hirata, F. Ab initio study of water. II. Liquid structure, electronic and thermodynamic properties over a wide range of temperature and density. *The Journal of Chemical Physics* **1999**, *111* (18), 8545-8555.
(81) Ohto, T.; Usui, K.; Hasegawa, T.; Bonn, M.; Nagata, Y. Toward ab initio molecular dynamics modeling for sum-frequency generation spectra; an efficient algorithm based on surface-specific velocity-velocity correlation function. *J Chem Phys* **2015**, *143* (12), 124702.
(82) Berens, P. H.; Wilson, K. R. Molecular dynamics and spectra. I. Diatomic rotation and vibration. *The Journal of Chemical Physics* **1981**, *74* (9), 4872-4882.
(83) Corcelli, S. A.; Skinner, J. L. Infrared and Raman line shapes of dilute HOD in liquid H2O and D2O from 10 to 90 degrees C. *J Phys Chem A* **2005**, *109* (28), 6154-6165.
(84) Auer, B. M.; Skinner, J. L. IR and Raman spectra of liquid water: theory and interpretation. *J Chem Phys* **2008**, *128* (22), 224511.
(85) Arntsen, C.; Chen, C.; Calio, P. B.; Li, C.; Voth, G. A. The hopping mechanism of the hydrated excess proton and its contribution to proton diffusion in water. *J Chem Phys* **2021**, *154* (19), 194506.
(86) Ishiyama, T.; Imamura, T.; Morita, A. Theoretical studies of structures and vibrational sum frequency generation spectra at aqueous interfaces. *Chem Rev* **2014**, *114* (17), 8447-8470.

(87) Morita, A.; Hynes, J. T. A Theoretical Analysis of the Sum Frequency Generation Spectrum of the Water Surface. II. Time-Dependent Approach. *The Journal of Physical Chemistry B* **2001**, *106* (3), 673-685.
(88) Nihonyanagi, S.; Mondal, J. A.; Yamaguchi, S.; Tahara, T. Structure and dynamics of interfacial water studied by heterodyne-detected vibrational sum-frequency generation. *Annu Rev Phys Chem* **2013**, *64*, 579-603.
(89) Ji, N.; Ostroverkhov, V.; Tian, C. S.; Shen, Y. R. Characterization of vibrational resonances of water-vapor interfaces by phase-sensitive sum-frequency spectroscopy. *Phys Rev Lett* **2008**, *100* (9), 096102.
(90) Balzerowski, P.; Meister, K.; Versluis, J.; Bakker, H. J. Heterodyne-detected sum frequency generation spectroscopy of polyacrylic acid at the air/water-interface. *Phys Chem Chem Phys* **2016**, *18* (4), 2481-2487.
(91) Wen, Y.-C.; Zha, S.; Tian, C.; Shen, Y. R. Surface pH and Ion Affinity at the Alcohol-Monolayer/Water Interface Studied by Sum-Frequency Spectroscopy. *The Journal of Physical Chemistry C* **2016**, *120* (28), 15224-15229.
(92) Reddy, S. K.; Thiraux, R.; Wellen Rudd, B. A.; Lin, L.; Adel, T.; Joutsuka, T.; Geiger, F. M.; Allen, H. C.; Morita, A.; Paesani, F. Bulk Contributions Modulate the Sum-Frequency Generation Spectra of Water on Model Sea-Spray Aerosols. *Chem* **2018**, *4* (7), 1629-1644.
(93) Montenegro, A.; Dutta, C.; Mammetkuliev, M.; Shi, H.; Hou, B.; Bhattacharyya, D.; Zhao, B.; Cronin, S. B.; Benderskii, A. V. Asymmetric response of interfacial water to applied electric fields. *Nature* **2021**, *594* (7861), 62-65.
(94) Wang, Y.; Seki, T.; Liu, X.; Yu, X.; Yu, C. C.; Domke, K. F.; Hunger, J.; Koper, M. T. M.; Chen, Y.; Nagata, Y.; Bonn, M. Direct Probe of Electrochemical Pseudocapacitive pH Jump at a Graphene Electrode. *Angew Chem Int Ed Engl* **2023**, *62* (10), e202216604.
(95) Yamaguchi, S.; Tahara, T. Heterodyne-detected electronic sum frequency generation: "up" versus "down" alignment of interfacial molecules. *J Chem Phys* **2008**, *129* (10), 101102.
(96) Mamatkulov, S. I.; Allolio, C.; Netz, R. R.; Bonthuis, D. J. Orientation-Induced Adsorption of Hydrated Protons at the Air-Water Interface. *Angew Chem Int Ed Engl* **2017**, *56* (50), 15846-15851.
(97) Dimiev, A. M.; Alemany, L. B.; Tour, J. M. Graphene oxide. Origin of acidity, its instability in water, and a new dynamic structural model. *ACS Nano* **2013**, *7* (1), 576-588.